Geochemistry, Geophysics, Geosystems®

AGU ADVANCING EARTH AND SPACE SCIENCES

RESEARCH ARTICLE
10.1029/2024GC011707

Integrated Rock Mass Characterization of the Lower Continental Crust Along the ICDP-DIVE 5071_1_B Borehole in the Ivrea-Verbano Zone

J. Li[1], E. Caspari[1], A. Greenwood[1], S. Pierdominici[2], K. Lemke[3], M. Venier[4], J. Kück[2], L. Baron[3], M. Pistone[5], B. Petri[6], L. Ziberna[4], and G. Hetényi[3]

[1]Chair of Applied Geophysics, Montanuniversität Leoben, Leoben, Austria, [2]Helmholtz Centre Potsdam GFZ German Research Centre for Geosciences, Potsdam, Germany, [3]Institute of Earth Sciences, University of Lausanne (UNIL), Lausanne, Switzerland, [4]Department of Mathematics and Geosciences, University of Trieste, Trieste, Italy, [5]Department of Geology, University of Georgia (UGA), Franklin College of Arts and Sciences, Athens, GA, USA, [6]Institut Terre et Environment de Strasbourg, Université de Strasbourg, CNRS, UMR7063, Strasbourg, France

Key Points:

- The axial plane of the Massone antiform dips a few degrees to the west-northwest in the vicinity of the borehole 5071_1_B
- The cluster analysis of gamma and magnetic susceptibility logs agrees well with core lithologies given the notable spatial variability
- Velocities are consistent across the core, log and seismic scales, governed by brittle deformation and locally correlate with lithologies

Supporting Information:

Supporting Information may be found in the online version of this article.

Correspondence to:

J. Li,
junjian.li@unileoben.ac.at

Citation:

Li, J., Caspari, E., Greenwood, A., Pierdominici, S., Lemke, K., Venier, M., et al. (2024). Integrated rock mass characterization of the lower continental crust along the ICDP-DIVE 5071_1_B borehole in the Ivrea-Verbano Zone. *Geochemistry, Geophysics, Geosystems*, *25*, e2024GC011707. https://doi.org/10.1029/2024GC011707

Received 18 JUN 2024
Accepted 24 NOV 2024

Abstract The first borehole 5071_1_B of the ICDP-Drilling the Ivrea-Verbano zonE (DIVE) project in Italy, which intersects the Massone antiform, provides a unique opportunity to integrate downhole geophysical measurements with observations from 100% recovered drill core in rarely drilled lithologies. The objective of this study is to petrophysically and structurally characterize the rock mass and constrain factors influencing the seismic velocity in the lower continental crust. A comprehensive data set, comprising core, well log and vertical seismic profiling data, was collected. The structural analysis indicates that the axial plane of the intersected tightly folded antiform is slightly tilted at the borehole location and thus the borehole intersects the hinge zone at the top and its limb in the lower part of 5071_1_B. Numerous open natural fractures with variable dips and two dominant dip azimuthal orientations are identified along the borehole, which affect the electrical and acoustic properties. The velocities at the core, well log and seismic scale are consistent but lower than intrinsic seismic velocities of the lower continental crust, since they are not only affected by fractures but also by micro cracks at the 5071_1_B in situ conditions. A systematic lithology correlation is not evident for these properties. However, a cluster analysis of gamma ray and magnetic susceptibility logs shows an excellent agreement with the logged core lithologies in the presence of remarkable spatial variability. Furthermore, the main lithologies are grouped into three distinct clusters, suggesting two types of kinzigites with distinct magnetic and radiogenic properties.

Plain Language Summary The first borehole 5071_1_B of the ICDP-Drilling the Ivrea-Verbano zone (DIVE) project in Italy, which intersects a prominent fold structure, provides a unique opportunity to integrate downhole geophysical measurements with observations from 100% recovered drill core in rarely drilled rock types. This study aims to characterize the structural properties and rock types encountered in 5071_1_B as well as factors that influence seismic velocity in the lower continental crust. The structural analysis shows that the axis of the fold is tilted at the borehole location. This means that the borehole intersects its hinge zone at the top and its limb in the lower part of 5071_1_B. Many open fractures are found with different dip angles and two main orientations. These fractures affect the electrical and acoustic properties. Gamma ray and magnetic susceptibility logs are used in a geostatistical analysis to identify different rock types. The results match the rock types identified on the drill cores very well. The P- and S-wave velocities at the core, well log and seismic scale are consistent but lower than the velocities of the lower continental crust at great depth. This is because they are affected by fractures and microcracks at the 5071_1_B pressure conditions.

1. Introduction

The Ivrea-Verbano Zone (IVZ, Southern Alps, Italy) is the first terrain interpreted as an exposed section of the lower continental crust (Berckhemer, 1969; Fountain, 1976; Mehnert, 1975) and offers a unique opportunity to study deep lithologies, which are generally inaccessible or heavily tectonized and displaced from their original arrangement. Consequently, this exposed section has been a prime location to gain insights into the composition, structure, and evolution of the continental lithosphere and is regarded as a petrological reference (e.g., Brodie & Rutter, 1987; Fountain, 1989; Pistone et al., 2020; Quick et al., 1995). The IVZ is also associated with multiple geophysical anomalies, known as the Ivrea Geophysical Body (IGB), featuring prominent gravimetric (e.g., Kissling, 1984; Niggli, 1947; Scarponi et al., 2020; The ECORS-CROP Gravity Group, 1989), seismic (e.g.,

Diehl et al., 2009; Lu et al., 2018; Scarponi et al., 2024; The ECORS-CROP Deep Seismic Sounding Group, 1989) and magnetic anomalies (e.g., Kissling, 1984; Lanza, 1982). These anomalies indicate that dense rocks of the lower continental crust and upper mantle are located at unusually shallow depths. The suspected proximity of upper mantle rocks to the Earth's surface makes the IVZ a prime candidate to drill for the first time through the geophysical Moho and the petrological crust-mantle transition zone, whereby the deepest, non-exposed portions of the IVZ crustal section can be directly assessed. The Drilling the Ivrea Verbano zonE (DIVE) project (ID: 5071), supported by the International Continental Scientific Drilling Program (ICDP), aims to achieve this by drilling three boreholes in two phases to sample the lower continental crust and the crust-mantle transition zone in the IVZ (Pistone et al., 2017). The two boreholes of Phase I at Ornavasso and Megolo in Val d'Ossola are intended to provide a continuous representative section of lower crustal lithologies and may encounter a transition into deeper mantle rocks. The first borehole 5071_1_B located in Ornavasso was completed in December 2022 and is the focus of this study. Altogether, the boreholes can provide an excellent opportunity to constrain the origin of geophysical anomalies and their correlation to deep crustal lithologies in the IVZ. Moreover, they may also offer important constraints on geophysical expressions of these lithologies in other areas, where surface geophysical measurements provide the only means to investigate these lithologies at depth.

Signatures of lower crustal lithologies in surface geophysical investigations can be ambiguous, especially the origin and nature of reflective seismic energy in the lower continental crust is poorly understood (Mooney & Meissner, 1992). To constrain the interpretation of surface geophysical data, outcrop data provides a valuable source of information. A number of outcrop core measurements including seismic velocities, density (e.g., Barruol & Kern, 1996; Chroston & Simmons, 1989; Fountain, 1976; Kern & Schenk, 1985; Khazanehdari et al., 2000), and magnetic susceptibility (e.g., Wasilewski & Fountain, 1982; Williams et al., 1985) have been conducted to constrain the variability of these properties across different lithologies in the IVZ. In combination with geometrical information from exposed crustal cross-sections, geophysical models have been created and tested to guide the interpretation of surface geophysical measurements in the IVZ (e.g., Scarponi et al., 2020; Scarponi et al., 2021). Constructed 1D and 2D seismic models indicate that lithologic layering or elastic anisotropy could be responsible for seismic reflections in the lower continental crust (Burke & Fountain, 1990; Goff & Holliger, 2003; Hale & Thompson, 1982). However, other factors contributing to seismic reflectivity of the lower crust cannot be excluded, such as for example, compositional variability controlled by mineralogical to lithological banding, the presence of shear zones and/or fluid-filled fracture zones, intrusions/dykes, and/or scattering from stochastic velocity or density distributions (e.g., Smithson et al., 2000). A drawback of populating models with physical properties measured on outcrop core samples or using them to constrain the interpretation of geophysical data is that they only provide point information at the centimeter scale and are often quite scattered over an area, rather than providing a continuous record across lithologies. As a result, the appropriate scaling of physical properties measured on core samples remains challenging to capture a representative level of heterogeneity of the continental crust at the spatial scale of meters, hundreds of meters, or even kilometers. Consequently, linking a specific physical property averaged over the scale of the surface measurement at hand directly to rock composition often remains ambiguous or impossible, as pointed out for the IGB by Pistone et al. (2020).

Geophysical borehole measurements allow to bridge this gap in spatial scales. Borehole logging methods provide continuous, high-resolution profiles of key physical and structural parameters (Ellis & Singer, 2007). Vertical seismic profiling (VSP) records seismic wavefield components at the source of origin of reflection events. An integrated analysis of a set of borehole logs and VSP data coupled with the information from drilled cores can provide a direct link between geological features and seismic properties by bridging the two very different scales of core and surface seismic observations. While an integrated analysis has become a standard for sedimentary settings (e.g., Bloomer & Mayer, 1997; Miller et al., 2013), it is still rarely applied in metamorphic and igneous settings, especially for lower crustal rocks. An obvious reason is that there are fewer boreholes in these lithologies and most of these are restricted to upper to mid-crustal rock: for example, the Kola Superdeep Borehole (KSDB) (Kozlovsky & Adrianov, 1987), the KTB borehole of the German Continental Drilling Program (Emmermann & Lauterjung, 1997), the Chinese Continental Scientific Drilling Program in the Dabie-Sulu orogen (e.g., Xu et al., 2017), and the COSC boreholes in central Scandinavian Caledonides (Lorenz et al., 2015). An additional complication is that core-log-seismic integration methods have been largely focused on granular sedimentary environments and their pore space structures (e.g., Avseth et al., 2005; Ellis & Singer, 2007; Tiab & Donaldson, 2015). As opposed to these formations, lower crustal rocks are primarily characterized by their mineral and chemical composition, metamorphic grade, texture and fabric, as well as deformation features (Waters et al., 2003). Matrix porosities are in

general very small and fluid pathways are mostly associated with brittle deformation structures ranging from micro-cracks, smaller than a millimeter, to fractures on the millimeter to the meter scale (e.g., Barton & Stephansson, 1990). Micro-cracks substantially contribute to the stress-sensitive behavior of rocks and thus affect velocities measured under different pressure conditions (Popp & Kern, 1994). Consequently, an integrated rock mass characterization of low porosity metamorphic and intrusive rocks across scales has to be adapted to separate mineralogical factors, from texture and brittle deformation impacts as well as pressure effects. To date only a few rock mass characterization studies based on core and borehole data have been conducted in hard-rock environments using multivariate statistical methods, for example, in mineral exploration settings (Kitzig, 2018; Mahmoodi & Smith, 2015), in crystalline environments characterized by brittle deformation structures (Caspari et al., 2020) and scientific drilling projects in metamorphic rocks such as the KTB borehole (e.g., Maiti & Tiwari, 2010; Pechnig et al., 1997), at the Deep Fault Drilling Project in New Zealand (Townend et al., 2013), and the COSC-1 borehole (Elger et al., 2021). In general, these studies show that nuclear and magnetic susceptibility borehole logs are sensitive to the rock's composition, whereas electrical and acoustic logs are sensitive to brittle deformation, rock texture and mineralogy. Linking these factors to the observed seismic properties (e.g., velocity variations) in the vicinity of the borehole is an essential prerequisite to constrain the origin of seismic reflectivity. For the COSC-1 borehole, Kästner et al. (2020) successfully constrained the origin of velocity variations by correlating core and VSP velocities with lithological and structural characteristics inferred from the cored rocks. A similar approach has been successfully applied to constrain the origin of velocity variations in the CCSD (Sun et al., 2012), KTB (Lüschen et al., 1996) and Kola borehole (Vernik et al., 1994).

The main objectives of this study are to characterize the rock mass and constrain the factors that influence seismic velocity variations in lower crustal rocks encountered in borehole 5071_1_B, based on geophysical borehole measurements and information from drilled cores. The characterization of the rock mass is divided into two parts: structural and lithological. This two-step approach enables a systematic analysis of the structural and lithological impact on the in situ measured physical properties, which in turn can then be consistently correlated to seismic properties. To further constrain the influence of these factors on seismic velocities, we investigate velocities inferred at three different scales, namely the core, log and VSP scales. The paper is structured as follows. First, the geological setting is outlined with the relevant lithologies. This is followed by a brief data overview, including the data acquisition and relevant processing steps for the different data sets. Next, the methods used for the rock mass characterization are summarized. The results of the structural and lithological rock mass characterization and the velocity comparison across scales are then presented. Finally, the results are discussed with respect to their structural and lithological implications and their consequences for seismic reflections in borehole 5071_1_B.

2. Geological Setting

The IVZ (Figure 1) is a block of preserved lower continental crust of the Adriatic plate located in the north-western Italian Alps (Berckhemer, 1969; Decarlis et al., 2023; Fountain, 1976). It is exhumed to the surface and exhibits a NE-SW trend and a steeply dipping layered structure (Barruol & Kern, 1996; Malusà et al., 2021; Peressini et al., 2007). The north-western boundary of the IVZ is marked by the Insubric Line, which is a major Alpine fault that separates the Western and Central Alps (European Plate) to the North-West from the Southern Alps (Schmid et al., 1987). In the south-east, the IVZ adjoints against the upper crustal rocks of the Strona-Ceneri zone and is separated by the Cossato-Mergozzo-Brissago (CMB) Line and the Pogallo Line (e.g., Handy, 1987; Zingg, 1983). The rocks of the IVZ can be subdivided into three main geological domains comprising lower crustal rocks: the Kinzigite and Stronalite formations, the Mafic Complex, and several embedded mantle peridotite slivers. The Kinzigite and Stronalite formations consist mainly of amphibolite (Kinzigite) to granulite facies (Kinzigite and Stronalite) metasedimentary rocks, with minor amounts of calcsilicate paragneiss, marbles and amphibolites (Henk et al., 1997; Quick et al., 2003; Schnetger, 1994). The Mafic Complex comprises mainly gabbros and norites, with minor amounts of diorites and charnockites, and is interlayered with and underlying the rocks of the Kinzigite formation (Quick et al., 2003; Sinigoi et al., 1991, 1994). Peridotites consist of several ultramafic bodies of lithospheric mantle material outcropping along the north-west margin of the IVZ (Quick et al., 1995; Sinigoi et al., 1994). The Kinzigite formation records Permian high-grade regional metamorphism, the metamorphic grade of which increases from amphibolite facies in the southeast to granulite facies in the northwest (e.g., Ewing et al., 2013; Rivalenti et al., 1981; Zingg, 1983). A second metamorphic event caused by the emplacement of the Mafic Complex led to high-temperature contact metamorphism forming a ∼2-km wide

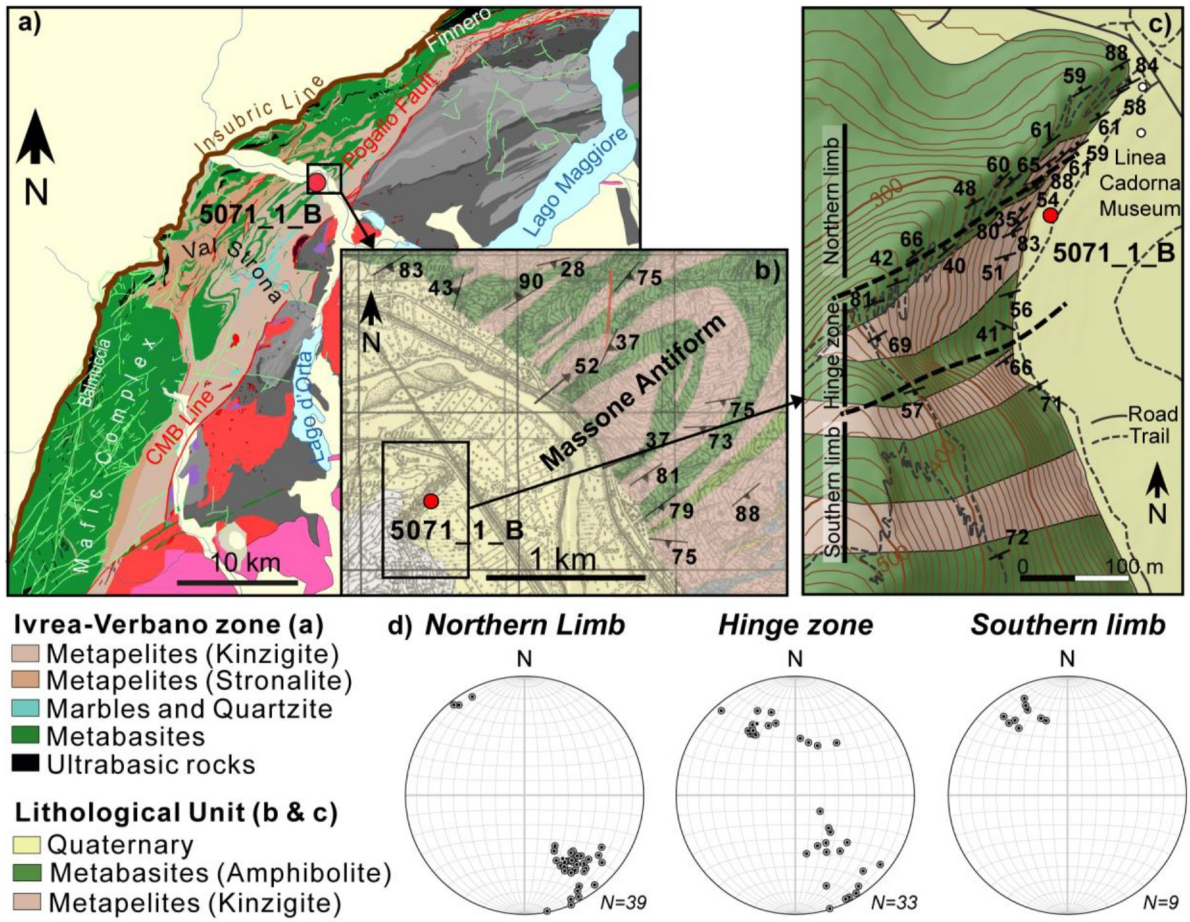

Figure 1. (a) Overview map of the Ivrea-Verbano Zone and adjacent lithological units (modified after Brack et al., 2010). (b) Section of the regional geological map from Burlini (2008) (modified after Schmid, 1967) near borehole 5071_1_B on the NE and (c) a mapped outcrop of the antiform in the vicinity of 5071_1_B on the SW side of Val d'Ossola. The red dot indicates the location of 5071_1_B. In panels (b, c) the black lines indicate the strike of the mapped outcrop foliation and the number the respective dips, and the arrows indicate direction of the mineral lineation. The mapped foliation of (c) is shown in panel (d) as poles to foliation planes in lower hemisphere equal area projection.

contact aureole around the mafic pluton (Barboza et al., 1999; Ewing et al., 2013; Peressini et al., 2007; Redler et al., 2012; Voshage et al., 1990).

The borehole 5071_1_B is situated in Val d'Ossola (Figure 1), which lies in the eastern-central part of the IVZ. The borehole intersects pre-Permian lithologies of the upper part of the lower continental crust in the domain of the Massone antiform, which is a large-scale fold traced for some 40 km along strike in the IVZ (Rutter et al., 2007). Its axis plunges approximately 30° NE to the NE of Val d'Ossola and outcrops as an upright near-isoclinical antiformal fold (Rutter et al., 2007). At the drill site 5071_1_B in Ornavasso, the antiform outcrops on both sides of the valley (Figures 1b and 1c) and its isoclinal closure outcrops at the summit of Cima Corte Lorenzo on the NE side suggest a vertical axial plane. The mapped foliation on the outcrop adjacent to the drill site of the northern and southern limbs of the antiform is steeply dipping (Figure 1c). The borehole is aimed at the hinge zone of the antiform to intersect a succession of alternating bands consisting of metasediments of the Kinzigite formation and hornblende-plagioclase amphibolites (Rutter et al., 2007). The outcropping metapelites are composed of garnet, biotite, plagioclase, quartz and minor amounts of sillimanite and muscovite. The garnet-bearing metasediments of the IVZ are enriched in U, Th and K compared to mafic and ultramafic rocks (e.g., Bea & Montero, 1999; Redler et al., 2012; Williams et al., 2022) and occasionally show leucocratic layers (leucosomes). An increase in metamorphic grade is indicated by the replacement of muscovite (and quartz) with K-feldspar and an increase in garnet content. Higher-grade metapelites are interlayered with amphibolite bands (Rutter et al., 2007). Amphibolites in the IVZ can be associated with high magnetic susceptibilities in the presence of

magnetite, whereas the metapelitic rocks of the Kinzigite formation are generally characterized by low susceptibilities and the most likely magnetic mineral present is pyrrhotite (Belluso et al., 1990). The susceptibility categories low (<1,500 10^{-6} SI), intermediate (4,000–8,000 10^{-6} SI) and high (>29,000 10^{-6} SI) are defined after Belluso et al. (1990).

3. Materials and Methods

3.1. Data Overview, Acquisition and Processing

The borehole is drilled to a depth of 578.5 m below the ground (geological reference) into the Massone antiform using the wireline continuous coring technique. Full recovery (100%) of the rock cores was successfully carried out. The rock cores contain a succession dominated by kinzigites (73%), amphibolites (13%), calcsilicates (11%), with leucosomes in places (3%), as identified using visual core description during the DIVE sampling party in 2024. Figure 2 shows the corresponding lithology column along the borehole track.

The borehole was drilled in a telescopic style, with SQ (borehole diameter: 146 mm, depth: 0–40.6 m), PQ (borehole diameter: 123 mm, depth: 40.6–316 m) and HQ (borehole diameter: 96 mm, depth: 316–578.5 m) sections (Figure 2). Our database includes a suite of geophysical downhole measurements, including natural radioactive, electrical, magnetic, acoustic and imaging logs as well as vertical seismic profile data (VSP). To complement the borehole data set, bulk density measurements on 96 core sections were obtained using a multi-sensor core logger (MSCL), and laboratory measurements of bulk density and P- and S-wave velocities on 15 core samples were performed under ambient conditions. Their depth locations are indicated in Figure 2.

3.1.1. Downhole Logging

The downhole logging was conducted in multiple campaigns for borehole 5071_1_B. The first two logging campaigns were performed when the borehole reached a depth of 316 and 500 m. The collected data sets comprise natural gamma ray (GR), magnetic susceptibility (MS), mud parameter (MP) and acoustic televiewer (ATV) data. The purpose of these logging campaigns was to support the interpretation of the midway VSP data. After the completion of the drilling activities in December 2022, a more comprehensive set of borehole logs was collected comprising natural gamma ray, dual laterolog resistivity (DLL), MS, MP, two-receiver full waveform sonic (FWS), and ATV measurements. The borehole log set was complemented in June 2023 with optical televiewer (OTV), single point resistance (SPR), and additional four-receiver FWS data. Figure 2 illustrates the depth range covered by each log. Not all borehole logs are of sufficient quality for the analysis over the full depth range or collected over the full depth range (Figure 2). The MP data were acquired only from the bottom up to 96 m depth. The OTV data is only of good quality to characterize geological features and fractures in the interval from 449 to 575 m depth. Beyond this depth, the borehole fluid was contaminated with the drilling polymer, which prevented obtaining optical images of sufficient quality. Shear wave velocities are only retrieved in the HQ section of the borehole. The excitation of shear waves by a monopole source relies on constructive interference, which is dependent on the transmitter frequency, borehole diameter and formation velocity (Hearst, 2000). The FWS measurements with the two-receiver sonde at a fixed transmitter frequency of 10 kHz with a monopole source did not excite shear waves. With the four receiver FWS sonde, which has selectable transmitter frequencies (10–30 kHz), shear waves could be excited in the HQ section of the borehole; however, it was not possible to obtain shear wave signals of sufficient signal strength in the PQ section of the borehole.

A quality control, depth matching and standard data processing are performed for all logs. The borehole logs collected with the ICDP operational support group tools are depth matched utilizing the gamma ray measurements, as each sonde was run combined with a total-GR sensor. The borehole logs collected with the tools from the University of Lausanne are depth matched using a combination of FWS, DLL and ATV data and their characteristic responses to fractures as reference points. Standard processing of the OTV and ATV image logs includes orientation to the magnetic north and bad trace interpolation for skipped or incomplete measurements. Only a few bad traces are present in the data sets. To enhance geological features for the OTV images in the depth section of 449–575 m, the brightness and contrast are adjusted. The ATV images are centralized with respect to the borehole axis and static and dynamic processing is applied to improve the image quality and enhance geological structures for easier interpretation (Williams & Johnson, 2004). The P-wave velocity is determined from the FWS data by manually picking the first arrivals of the compressional waves of each receiver. The velocity is estimated between pairs of consecutive receivers, and the resulting slownesses are averaged at

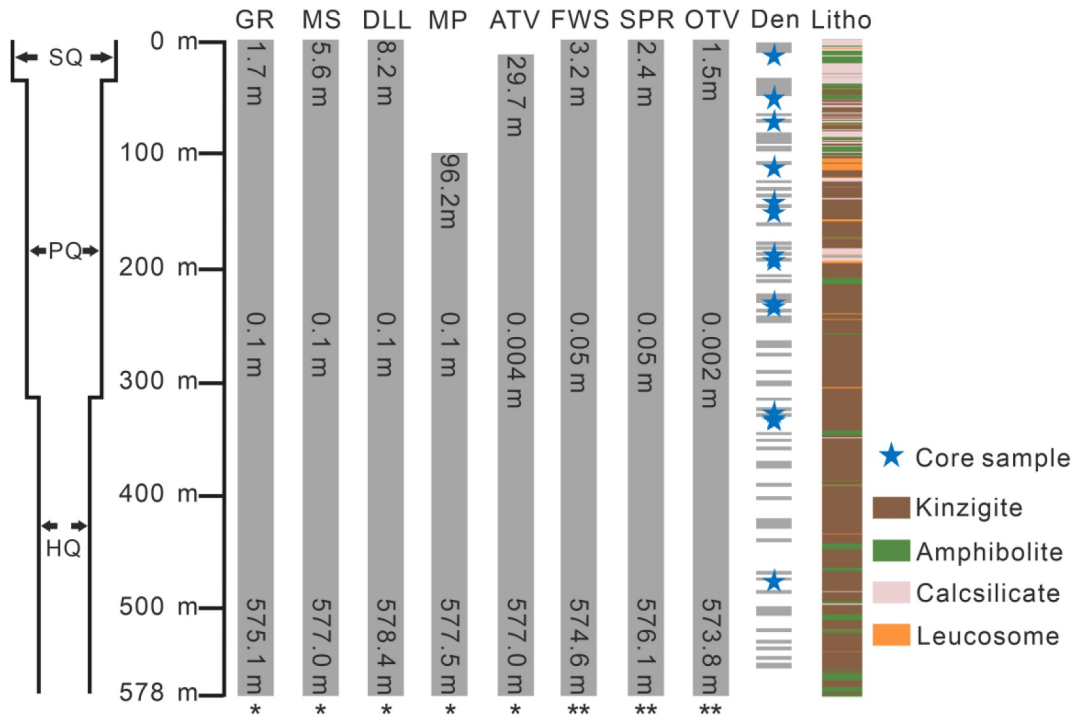

Figure 2. (a) Wellbore schematic of 5071_1_B (leftmost column), from left to right: depth coverage of the borehole tools, with the abbreviations: GR: natural gamma ray, MS: magnetic susceptibility, DLL: dual laterolog resistivity, MP: mud parameter including mud resistivity, temperature and pressure, ATV: acoustic televiewer, FWS: full waveform sonic, SPR: single point resistance and OTV: optical televiewer. The top and bottom numbers indicate the logging end and start depths, respectively, and the middle number indicates the sampling interval. This is followed by the depth location of the 96 core sections for multi-sensor core logger density measurements (Den) and 15 core samples for laboratory measurements as well as the core lithology (Litho). * tools from the ICDP-Operational Support Group, ** tools from the University of Lausanne.

common depth points to increase the robustness of the estimate. The S-wave velocity is obtained by conducting a semblance analysis (Mari, 1994) over the last three receivers. This results in a higher fidelity for the P-wave velocity than for the S-wave velocity, which provides an average estimate over three receivers.

3.1.2. Vertical Seismic Profiling

Vertical seismic profiling data were collected during the first logging campaign and after the completion of drilling activities of borehole 5071_1_B. The midway VSP campaign was conducted at 316 m depth to assess the orientation of the borehole with respect to the hinge zone and limbs of the Massone antiform. For both VSP campaigns, a 400 kg weight-drop source and a three-component geophone chain consisting of five geophone levels with a 10 m level spacing were utilized. To increase the spatial resolution, the data were collected in 5 m depth increments from 570 to 30 m. Four offsets were acquired at 10, 100, 200, and 400 m, respectively. The 10 m offset is used as the zero offset shot point. At each depth step, four seismic shots were performed for each offset position. The upper 50 m (30–80 m) of the borehole was acquired with a hammer source. The acquisition parameters are summarized in Table 1.

Table 1
VSP Acquisition Parameters

Tool	SGC SlimeWave geophone chain
Receiver type	15 Hz, 3 components
Level number	5
Level spacing	10 m
Sampling rate	1 ms
Recording length	1 s
Source type	400 kg tractor mounted weight-drop
Offset	10, 100, 200, 400 m

For this study, the P-wave and S-wave interval velocities of the zero-offset VSP data (ZVSP) are of interest. For this purpose, the following processing steps are applied. The data is resampled to a sampling rate of 0.1 ms for accurate first break picking. Static time shifts are applied to individual shot records to compensate for arrival time variations between consecutive shots at the same source location due to ground compaction. The resulting shot records for each source location are stacked to improve the signal-to-noise ratio.

To estimate S-wave velocities, the horizontal components (H1 and H2) are rotated to the radial and transverse directions with respect to the source location using a hodogram analysis which is performed for the offset shot at 100 m, offering a more robust orientation of the horizontal components than utilizing the ZVSP shot location. The rotation angles were then applied to the zero-offset data, which is used for the velocity analysis. The shear wave velocity is obtained from the rotated horizontal component H1, which contains more coherent and higher amplitude S-wave arrivals than component H2. To improve the signal-to-noise level of the data for manual picking of P- and S-wave arrivals, FK polygon pass filters (with the parameters f ∈ [0 410] Hz, k ∈ [−0.45 0.02] rad/m for P-waves and f ∈ [0 186] Hz, k ∈ [−0.38 0.02] rad/m for S-waves) are applied to remove low-frequency noise before the P-wave first arrivals and to reduce wavefield interference at the onset of the S-waves. The final velocities are calculated for 10 m depth intervals, since the interleaved data sets with 5 m spacing contained inconsistencies which could not be sufficiently suppressed with static corrections. Furthermore, a more robust interval velocity over the length of the geophone string corresponding to 40 m is calculated.

3.1.3. Core Measurements

The downhole geophysical measurements are complemented by petrophysical core measurements, which comprise magnetic susceptibility of the recovered core, MSCL density of 96 core sections (see Appendix A) as well as ultrasonic velocity and bulk density laboratory measurements on 15 selected whole-round core samples. The main purpose of the magnetic susceptibility measurement is to correlate the core and borehole log depths for an integrated analysis of core observations and borehole log attributes. The magnetic susceptibility was measured along the entire recovered core on-site during the drilling operation at 10 cm intervals using the Bartington MS2 magnetic susceptibility meter with a loop sensor of 133 mm diameter. Drill core diameter corrections were automatically applied. The MSCL density measurements were conducted as a substitute for a density borehole log, whereby 96 selected core sections with a total length of 56.8 m at a spatial interval of 0.02 m under ambient conditions were measured with a Cs-137 gamma-ray source during the first preliminary sampling party. The data were calibrated with laboratory bulk density measurements from the 15 selected core samples (Appendix A).

A total of 15 whole-round core samples (Table B1) of approximately 10 cm in length were selected for petrophysical measurements under ambient conditions. The bulk density is determined by utilizing Archimedes' principle from the following equation:

$$\rho_c = m_c \rho_w / (m_c - m_{\text{sub}})$$

where ρ_c is the core bulk density, m_c is the mass of the dry core, ρ_w is the water density, m_{sub} is the apparent mass of the dry core submerged in water. The samples were dried in an oven at 50°C for 24 hr before the dry mass m_c was measured. Subsequently, the core sample was submerged in water to determine the apparent mass m_{sub}. Dry and saturated ultrasonic P- and S-wave velocities were measured using P- and S-wave transducers at 1-MHz frequency under ambient conditions. For the ultrasonic experiments, core samples featuring rough or irregular ends were cut to improve the coupling between the transducers and the core. To further improve the coupling, a small axial pressure of 3 bar and a coupling agent were utilized. To saturate the samples, they were first placed under vacuum in a desiccator and then saturated with water in the same desiccator for 2 days. The velocities are determined from the automatic and manual picked travel times of P- and S-waves.

3.2. Rock Mass Characterization

The rock mass characterization is performed in a two-step approach, which enables a systematic analysis of the structural and lithological factors that influence the in situ physical properties. First, a structural characterization is carried out based on ATV image, electrical, and FWS logs. This is followed by an integrated analysis of core lithologies and borehole log data to characterize the rock mass from both a lithological and petrophysical standpoint.

3.2.1. Structural Characterization

ATV images yield a continuous record of structures that intersect the borehole, such as fractures, layering, and faults, and provide detailed information on their location, orientation (dip azimuth and dip), and occurrence intensity. Electrical and FWS logs provide complementary information to these geometrical characteristics about the physical properties of fractures, as they are sensitive to their hydraulic and mechanical properties. Borehole

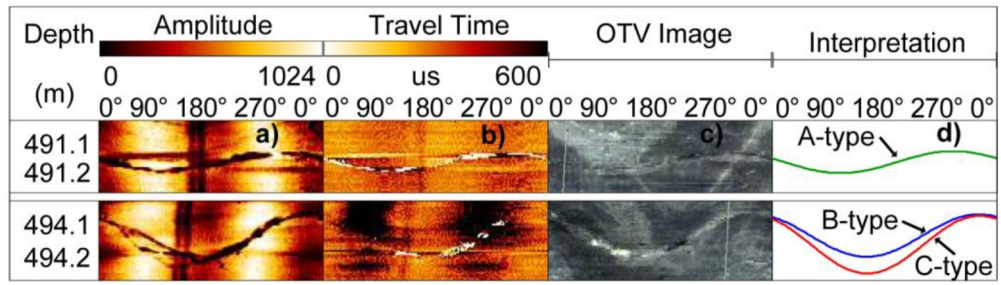

Figure 3. Features of A-, B- and C-type fractures. (a) ATV amplitude image. (b) ATV travel time image, (c) OTV image. (d) Fracture interpretation (0° is the magnetic north).

breakouts observed in ATV images, created during the drilling process due to stress-induced borehole failure, are indicative of the stress state around the borehole.

The ATV provides 360° high-resolution, magnetically oriented, color unwrapped acoustic amplitude images of the surface reflectivity of the borehole wall and acoustic travel time images of a fluid-filled borehole (Zemanek et al., 1969). The travel times are representative of the borehole shape, whereby long travel times reveal borehole enlargements. In the amplitude image, high amplitudes correspond to a strong contrast between the rock mass and borehole fluid, indicating a competent rock mass, whereas weak to missing signals are indicative of open fractures, voids, and breakouts. In this study, fractures are classified into three types according to their visual appearance on the images, corresponding to their amplitude contrast and travel-time difference with respect to the surrounding rock mass. A- and B-type fractures exhibit a high amplitude contrast and are completely (A) or partially visible (B) in the travel time image, respectively, whereas C-type fractures are only moderately or weakly visible in the amplitude image. Figure 3 shows an example of the three fracture types identified in the ATV amplitude and travel time images as well as their expression on the OTV image.

All structures that intersect the borehole appear as sinusoidal features on the ATV images from which the dip and dip azimuth (or dip direction) are estimated. To obtain the true orientation, the dip and dip azimuth are recalculated based on the caliper, tilt and azimuth of the borehole (Paillet et al., 1985, 1990). To quantify the occurrence intensity of fractures along the borehole, fracture densities are calculated over a moving average window. The fracture density is defined as $D_f = n/L$, where L is the window length, and n is the number of fractures in the corresponding section. Borehole breakouts form borehole enlargements at diametrically opposite sides of the borehole, where the local compressional stress exceeds the compressive strength of the rock (e.g., Zoback et al., 1985). If the borehole is vertical and parallel to the vertical principal stress, the maximum compressional stress at the borehole wall builds up along the minimum horizontal principal stress axis (e.g., Bell & Gough, 1979; Zoback et al., 1985). Breakouts are identified on the ATV image by their symmetrical pattern of long travel times and low amplitudes (Lofts & Bourke, 1999). The depth, length, azimuth and opening angle of breakouts are evaluated on the processed ATV images. The azimuth of the breakout indicates the minimum horizontal principal stress orientation under the aforementioned stress conditions, while the opening angle corresponding to the breakout width is indicative of the stress magnitude (Barton et al., 1988).

Electrical logs recorded in resistive formations, such as metamorphic rocks, are highly sensitive to open water-filled fractures because of the strong electrical contrast between the rock mass and the fluid in fractures. Open water-filled fractures occur in these logs as low resistivity anomalies and are indicative of the fluid flow pathways in the encountered rock mass. Owing to the different logging tool geometries, the DLL has a higher vertical resolution than the SPR tool. The former responds to open fractures, while the latter predominantly detects distinct fractures with larger apertures and extensive lengths. In FWS data, the occurrence of a mechanically compliant fracture or fracture zone between the transmitter and receiver of the tool results in acoustic travel time delays and amplitude decays. Here, we utilize the acoustic travel time delays of the first P-wave arrivals to identify such mechanically compliant fractures. Details are provided in the Text S2 in Supporting Information S1. These travel time delays lead to local low P-wave velocity anomalies. To a first order, the magnitude of time delays and resulting P-wave velocity anomalies is determined by the normal fracture compliance (Zhou et al., 2022).

3.2.2. Lithological and Petrophysical Rock Mass Characterization

The data structure of the petrophysical properties, obtained from the borehole logs, of the two dominant core lithologies is analyzed using histograms and crossplots. This allows us to identify whether the borehole log responses can be linked to the core lithologies and examine the correlations between different petrophysical properties. Based on this analysis, a set of borehole logs is selected for fuzzy c-means clustering to categorize the data into groups according to their petrophysical characteristics. Fuzzy c-means clustering is an unsupervised machine learning method, which groups the data into clusters based on probabilities calculated from the distance between each point and cluster centers through a minimization process (Bezdek et al., 1984). The closer the probabilities of a single point with respect to different clusters are, the fuzzier the clustering result is. In this study, we utilize the fuzzy c-means clustering algorithm implemented by Kitizg (2018). For fuzzy c-means clustering two key parameters have to be chosen: the cut-off value α, and the weight exponent m, which determine how hard or soft the cluster boundaries are. The cut-off value for the membership degree is defined (Yang et al., 2008), such that a sample with a membership value above α is assigned to one unique cluster and a value below α results in the sample belonging to more than one cluster at the same time (non-uniquely assigned). Larger values of m and α result in fuzzier or soft cluster boundaries while smaller values specify hard boundaries. For the cluster analysis, the data is standardized, since petrophysical properties have very different units and scales and their absolute values span several orders of magnitude. Here we use a Z-score standardization $Z = (x - \mu)/\sigma$, where x is the petrophysical property, μ its mean value and σ the standard deviation of the property (Abdi & Williams, 2010). The fuzzy c-means clustering itself is performed in two subsequent steps. First, the optimal cluster number to group the data into is determined. In this study, we utilize the silhouette criterion, which measures how similar each point is to other points in the same cluster compared to points in other clusters in terms of the squared Euclidean distance (Kaufman & Rousseeuw, 2009). Then, the clustering algorithm is applied with the optimal cluster number.

4. Results

4.1. Structural Rock Mass Characterization

In total, 575 natural fractures are detected in the ATV images and their inferred geometrical characteristics are displayed in Figure 4. To quantify the occurrence of fractures along the borehole, one fracture density for A- and B-type fractures, and one for C-type fractures is calculated over a moving average window of 5 m. The resulting fracture densities are displayed in Figure 4c. C-type fractures are prevalent along the borehole track and the largest fracture densities occur in the intervals of 142–155 m, 330–340 m, 350–355 m and 365–372 m depths with 3.4, 3.6, 3.4 and 3.1 fractures/m, respectively, while A- and B-type fractures account only for 8.7% of the total number of fractures and are scattered along the borehole track. The estimated dip azimuths (Figure 4a) and dips (Figure 4b) of the 575 fractures are shown along the borehole track in the form of histograms in 5 m intervals. Two dominant dip azimuth orientation sets can be identified in Figure 4h, which are marked as red stripes in Figure 4a. The first set comprises 44.6% of the fractures and falls between N320° and N30° (NW to NE), while the second set encompasses 20% of the identified fractures and falls between N120° and N160° (SE to SSE). Fractures exhibit a wide range of dips. In the upper section, above 265 m depth (Figure 4b), fracture dips vary from 30° to 85°. In a short section between 265 and 330 m depth, fracture dips decrease to values smaller than 50°. The interval between 330 and 385 m depth contains an abundance of fractures, exhibiting the largest variability in dip angles, with values ranging from 10° to 80°. Below 385 m depth in the lower section of the borehole, most fracture dips fall below 45° and are on average smaller than those in the upper section.

Borehole breakouts occur only in the lower section of the borehole (Figure 4g). A total of 29 breakouts are identified in the depth interval of 355–555 m with a cumulative length of 11.78 m. They exhibit a mean azimuth of N145° (st.dev. = 12°) with no significant differences in orientation between the individual breakouts. The average opening angle of breakouts is 52.8° with a standard deviation of 13.8°. As such, breakouts do not induce significant borehole enlargements. Interestingly, they are only observed in the kinzigite sections and rarely intersected by fractures. This suggests that the present-day maximum horizontal principal stress orientation in the lower section of the borehole is parallel to the fracture planes, thereby keeping them open.

As expected for metamorphic rocks, the measured formation resistivity is high, with a median value of 9,300 Ω m and provides a strong contrast to the resistivity of the borehole fluid, which varies between 4.2 and 22 Ω m. This corresponds to the lower end of resistivity values for fresh groundwater (Suski et al., 2008; Tsang et al., 1990). Figure 4d presents the single point resistance and the resistivity log responses overlain on the A- and B-type fracture

10.1029/2024GC011707

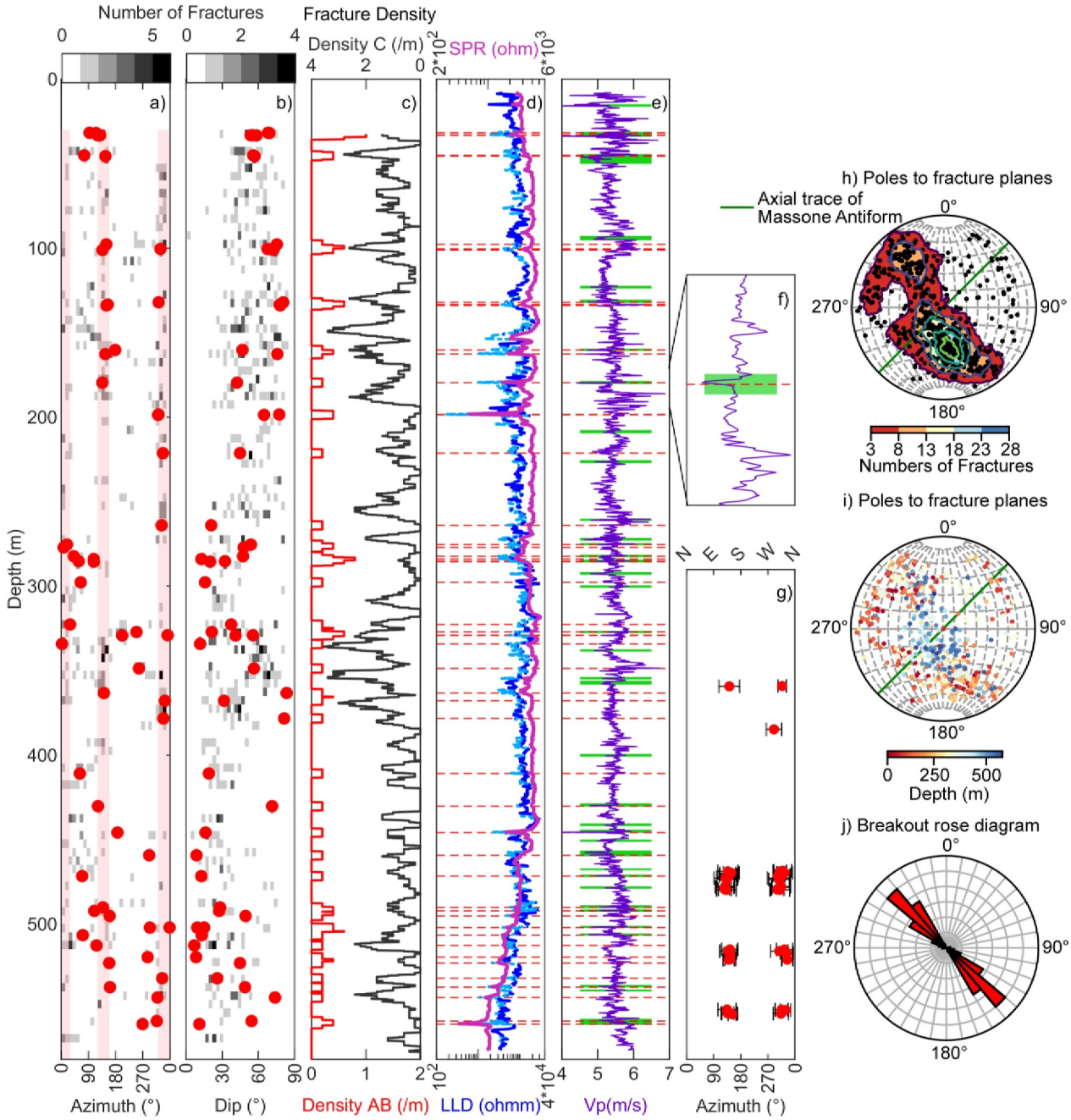

Figure 4. (a) Fracture dip azimuth and (b) fracture dip displayed in histographic form in 5 m intervals along the borehole. The two dominant dip azimuths are marked as red stripes and the dip azimuths and dips of A- and B-type fractures are indicated as red dots. (c) A- and B-type fracture density (red) and C-type fracture density (black). (d) Single point resistance (SPR) and deep laterolog resistivity (LLD), the resistivity anomalies are indicated by light blue dash-dots and the positions of A- and B-type fractures are marked as red dash lines. (e) Sonic P-wave velocity (v_p): fracture zones detected by the full waveform sonic are marked as green boxes and the positions of A- and B-type fractures are marked as red dash lines. (f) Zoom into the 170–190 m depth interval of v_p. (g) Borehole breakout orientation (red dots) and width (black segments). Lower hemisphere equal area projection of the poles (black dots) to the natural fracture planes with (h) Kamb contours and (i) color-coded by depth. The trace of the Massone antiform axial plane is indicated by the green line. (j) Rose diagram of borehole breakout orientations. 0° indicates the magnetic north in panels (h–j).

positions. The most pronounced low resistivity anomalies observed in both electrical logs are associated with these fracture types. Sections characterized by high fracture densities consisting of C-type fractures do not exhibit distinct and strong electrical anomalies, but show on average lower resistivities in the LLD log, for example, from 250 to 257 m. Conversely, the SPR log lacks indications of C-type fractures. In the FWS data, time delays and corresponding velocity anomalies of 37 fracture zones are detected and marked by green boxes in Figure 4e. A zoom-in of

a local velocity anomaly is shown in Figure 4f. Most zones show a good correlation with A- and B-type fractures and a few zones are located in C-type fracture intervals, such as the those at 121.8–122.8 m, 207.3–209.4 m and 475.3–478.8 m depths. There is a significant velocity anomaly caused by the fracture at 445.6 m depth with a P-wave velocity of 3.99 km/s. This is much lower than the velocity of the surrounding rock mass, which is 5.5 km/s.

All electrical anomalies related to 538 fractures (93.56% of all fractures identified on the ATV) in the borehole are likely to be caused by an electrically conductive fluid within the fractures. There is no indication of clay-filled fractures; however, a few of the fracture surfaces are covered with a thin graphite layer and/or sulfides, which may contribute to the low resistivity anomalies. Hence, most of these fractures provide hydraulic pathways through the rock mass. Some of these fracture zones act as active in-flow zones in the borehole. Details are provided in the Text S3 in Supporting Information S1. The magnitude of the velocity anomalies for the 37 fracture zones detected in the FWS, which include 114 fractures, is directly correlated to the normal fracture compliance. Fractures, which correlate with identified anomalies in the electrical and FWS sonic logs, making up 105 of all fractures (18.26%), are at least partially open, hydraulically conductive and characterize zones of mechanical weakness.

4.2. Lithological and Petrophysical Rock Mass Characterization

The data structure of the natural gamma radiation, magnetic susceptibility, sonic P-wave velocity and DLL resistivity of the two dominant core lithologies is analyzed using histograms and crossplots. For this analysis, a logarithmic data transformation is applied to the magnetic susceptibility and resistivity data, since their value range spans several orders of magnitude. The corresponding histograms and crossplots of the four petrophysical properties, color-coded by the core lithologies, are shown in Figure 5. The gamma ray data histogram (Figure 5a) exhibits a left-skewed distribution for the kinzigites, indicating a dominance of high gamma ray values. In contrast, amphibolites display a prevalence of lower gamma ray values with a right-skewed distribution. Calcsilicates exhibit a similar gamma ray distribution as amphibolites, but with a slightly higher mean value. There is a partial overlap between the three main lithologies for the gamma ray data. The magnetic susceptibilities of kinzigites have a right-skewed distribution, while both amphibolites and calcsilicates show left-skewed distributions with higher mean values (Figure 5c). There is a considerable overlap between the three lithologies for the magnetic susceptibility data. For the sonic P-wave velocity, the three lithologies exhibit a similar range of values between 5 and 6 km/s with almost completely overlapping symmetrical distributions (Figure 5f). The resistivity values of the kinzigites cover a wider range than those of the amphibolites and calcsilicates, which are completely encompassed by the values of the kinzigites (Figure 5j). On average, the resistivities of kinzigites are slightly higher than those of the amphibolites and calcsilicates. Overall, this suggests that the gamma ray and magnetic susceptibility responses are at least partially governed by the identified core lithologies. However, there is no clear correlation between the main identified core lithologies and the P-wave velocity and resistivity. To analyze the relationship between the petrophysical properties, we examine the crossplots. The gamma ray and magnetic susceptibility crossplot (Figure 1b) reveals two distinct trends: one for kinzigites and leucosomes and one for amphibolites and calcsilicates. Kinzigites exhibit a trend from low gamma ray and low magnetic susceptibility to high gamma ray and high magnetic susceptibility, whereas the amphibolites and calcsilicates show a trend from high magnetic susceptibility and low gamma ray to lower magnetic susceptibility and high gamma ray values. The two trends partially intersect each other. In all other crossplots associated with P-wave velocity and resistivity data (Figures 5d, 5e, 5g, 5h, and 5j), no distinct data trends or grouping of the data can be observed. Furthermore, the data clouds corresponding to the lithologies are mostly coinciding. Even though the P-wave velocity and resistivity seem to be affected by fractures, as discussed in Section 4.1, this is not reflected in a systematic trend in the crossplots between these two properties.

As only the gamma ray and magnetic susceptibility responses exhibit distinct data groups, these properties are selected for the cluster analysis. A moderate level of fuzziness is chosen with $m = 1.55$ and $\alpha = 0.55$. The fuzzy c-means clustering is performed on the standardized data for an optimal cluster number of 3 determined by the highest silhouette value. The results of the cluster analysis are displayed in Figure 6 as a crossplot for the standardized magnetic susceptibility and gamma ray data. The fuzzy area shows points whose membership values are below α and do not have a strong association to either of the three clusters. Overall, 62.43% of the data points are grouped into cluster 1, 21.52% into cluster 2%, and 13.35% into cluster 3. Cluster 1 is characterized by high magnetic susceptibility and natural gamma radiation, cluster 2 exhibits the highest magnetic susceptibility and a low natural gamma radiation, while cluster 3 is characterized by low magnetic susceptibility and natural gamma radiation. Hence, from a petrophysical standpoint, the data is grouped into three clusters. Cluster 1 and cluster 3

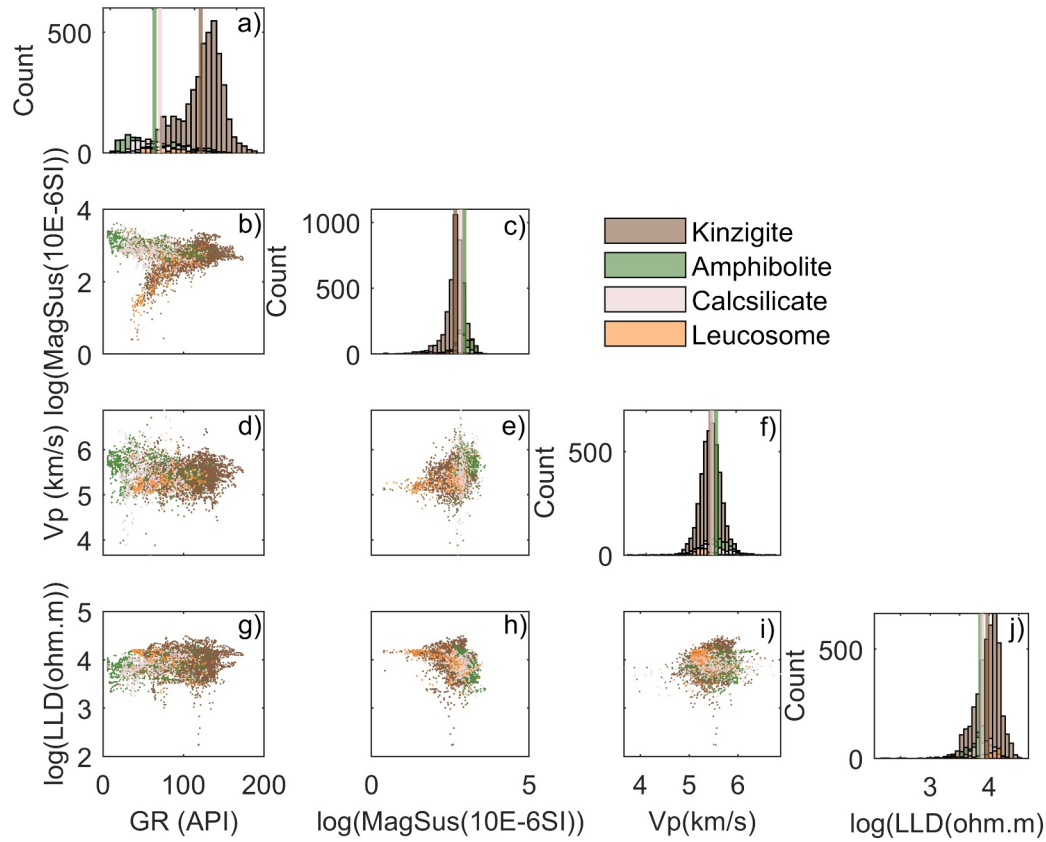

Figure 5. Histograms of borehole logs: (a) gamma ray (GR), (c) magnetic susceptibility (MagSus), (f) sonic P-wave velocity (Vp) and (j) deep laterolog resistivity (LLD). The brown, green and light pick lines in the histogram denote the mean value of the corresponding property for kinzigites, amphibolites and calcsilicates, respectively. Cross plots of borehole logs: (b) MagSus - GR, (d) Vp - GR, (e) Vp - MagSus, (g) LLD - GR, (h) LLD - MagSus and (i) LLD - Vp.

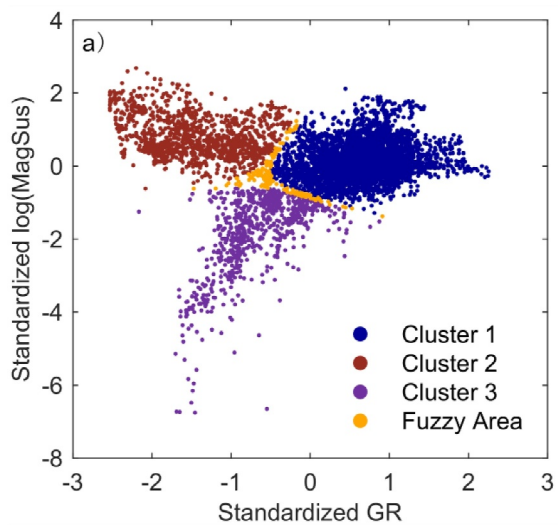

	AMPH	CALCS	KINZ	LEUCO	Cluster proportion
Cluster 1	3.00%	1.92%	56.57%	0.94%	62.43%
Cluster 2	9.68%	7.32%	4.16%	0.36%	21.52%
Cluster 3	0.12%	0.88%	10.42%	1.93%	13.35%
Fuzzy Area	0.30%	0.48%	1.75%	0.17%	2.70%
Lithology proportion	13.10%	10.60%	72.90%	3.40%	100.00%

Figure 6. (a) Crossplot of standardized magnetic susceptibility and gamma ray data color coded by the fuzzy c-means clustering results. (b) Percentages of the four lithologies for each cluster. AMPH: amphibolite, CALCS: calcsilicate, KINZ: kinzigite, LEUCO: leucosome.

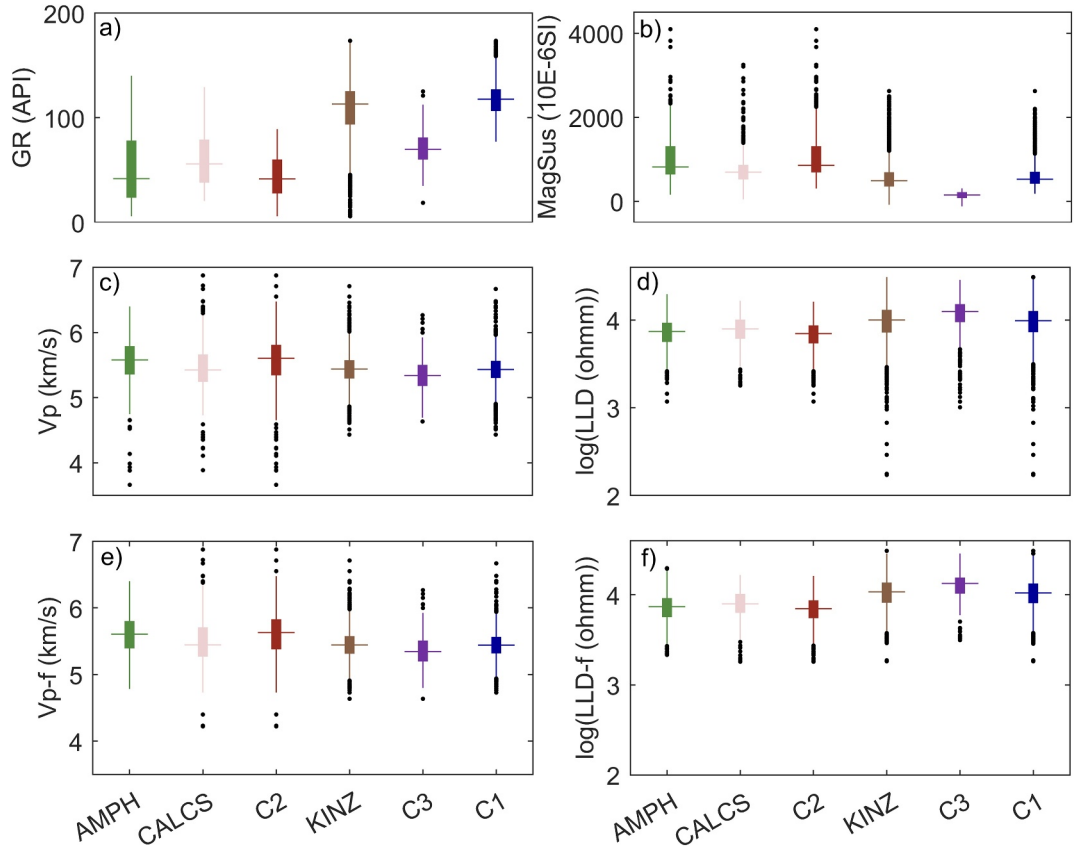

Figure 7. Box plots of amphibolites, calcsilicates, kinzigites and three clusters: (a) gamma ray (GR), (b) magnetic susceptibility (MagSus), (c) sonic P-wave velocity (Vp), (d) deep laterolog resistivity (LLD), (e) sonic P-wave velocity after the removal of fracture sections detected by full waveform sonic, (f) deep laterolog resistivity after the removal of fracture sections identified on the LLD log. AMPH: amphibolite, CALCS: calcsilicate, C2: cluster 2, KINZ: kinzigite, C3: cluster 3, C1: cluster 1. Median values are indicated as horizontal lines of boxes.

are primarily dominated by kinzigites with 56.57% and 10.42% of all data points belonging to this lithology falling into them, respectively. Cluster 2 is predominantly composed of amphibolites and calcsilicates, accounting for 9.68% and 7.32% of all data points. While 4.16% of all data points belonging to kinzigites fall into cluster 2, 3% and 1.92% of all data points belonging to amphibolites and calcsilicates are grouped into cluster 1. Leucosomes account for 3.4% of total data points and most of them fall into clusters 1 and 3. Figure 6b summarizes the distribution of the four lithologies among the three clusters.

To further compare the core lithologies and the three clusters, box plots of the petrophysical properties for the three main lithologies and the clusters are presented in Figure 7. For cluster 2, the median values of the gamma ray and magnetic susceptibility data are shifted to slightly lower and higher values, respectively, compared to the ones for amphibolites and calcsilicates. This is due to the fact that the high gamma ray amphibolites and calcsilicates fall into cluster 1. For the kinzigites, the core lithology boxplot and the two boxplots corresponding to clusters 1 and 3 highlight (Figures 7a and 7b) that two distinct groups of the kinzigites can be distinguished in the borehole with regard to their natural radioactivity and magnetic susceptibility. The median values for the gamma ray and magnetic susceptibility for kinzigites are 113 API and 493 10^{-6} SI, compared to 118 API and 527 10^{-6} SI for cluster 1 and 70 API and 152 10^{-6} SI for cluster 3.

P-wave velocities and resistivities have not been considered in the presented cluster analysis. However, tests including the two properties in the cluster analysis have shown no significant differences with regard to the three obtained clusters. This is not surprising since the crossplots indicate that there is no discrimination into distinct groups for these two properties. This is also corroborated by the boxplots in Figures 7c and 7d, which show no obvious differences in P-wave velocity and resistivity between the three main lithologies or between the three

clusters. To test whether fractures mask a lithological response for these two properties, the electrical and velocity anomalies associated with fractures in the ATV image, which are marked in Figures 4d and 4e, respectively, and discussed in Section 4.1, are removed from the data. A comparison of the resulting boxplots for velocities (Figure 7e) with those of Figure 7c reveals that apart from the removal of the low velocity outliers, no significant difference can be observed. This is consistent with the fact that the majority of the identified velocity anomalies are created by A- and B-type fractures, and constitute only 6.4% of all fractures. For the resistivities of the three main lithologies and three clusters, not only outliers are removed but the median values are slightly higher (Figure 7f) compared to the ones without removing the fracture anomalies. Compared to the velocity anomalies, the resistivity anomalies correspond to 77.9% of all fractures and thus their removal has some impact on the median values.

4.3. Velocity Comparison at Different Scales

In order to further constrain the factors influencing the velocities along the borehole, which ultimately define seismic reflection patterns, we compare the velocity at three different spatial scales: the core (0.1 m core size), sonic logging (0.3 m vertical resolution) and VSP (10 m spatial interval) scale. Figure 8 presents the corresponding P- and S-wave velocities obtained from the core measurements (Appendix B), the sonic logging data, and the VSP data. For the VSP data, the interval velocities corresponding to 10 and 40 m intervals are displayed. The sonic S-wave velocity was only retrieved in the HQ section. For comparison with the VSP data, upscaled sonic velocities to 40 m intervals are shown as well. The dry and saturated core velocities (Appendix B) at ambient conditions comprise 6 core samples classified as kinzigites, 4 as calcsilicates, 3 as amphibolites and 2 as leucosomes.

The P-wave velocities of the saturated cores from the sonic logging, and the VSP data fall between 5 and 6 km/s. The sonic and VSP S-wave velocities fall between 2.8 and 3.5 km/s in the HQ section of the borehole. Figures 8c and 8d compare the distribution of VSP and sonic velocities in the form of non-parametric density functions. The VSP velocities, are on average, slightly lower than the sonic velocities and exhibit a smaller variability. Along the borehole track, the 40 m interval VSP velocities generally match the upscaled sonic log velocities but are lower in some sections of the borehole, which is reflected in the overall lower mean velocity. The greater variability of sonic velocities can be attributed to the fact that the small-scale velocity variations detected by the FWS logs are averaged out in the VSP data, given that the wavelength is approximately 100 m in the VSP data compared to 0.3 m in the sonic data, corresponding to a vertical resolution of 25 and 0.075 m, respectively.

The saturated core and sonic P-wave velocities are in close agreement, particularly for six cores located between 100 and 250 m depth. In this instance, both measurements average the velocities over a similar support volume, given that the sonic P-wave wavelength is on the order of 0.3 m, which is approximately the geophone spacing and on a similar order as the core sample size. The three cores, 135_2, 137_3 and 138_1, which correspond to a kinzigite and two amphibolite cores, respectively, exhibit a similar velocity trend as the sonic log data. This suggests that the velocity data contain some lithological information. Indeed, the mean P-wave velocity of the saturated amphibolites is 5.86 km/s, which is slightly higher than the mean velocity of the kinzigites, which is 5.22 km/s Figure 8a also illustrates that there is a distinct difference between the P-wave velocity of the dry cores, which ranges from 3.6 to 4.8 km/s, and the saturated cores, which exhibit velocities of 4.8–6.1 km/s. The S-wave velocity difference between the dry and saturated cores is much smaller. It is noteworthy that above 316 m depth, the VSP S-wave velocities match the dry core S-wave velocities apart from Core 31_1 and 31_3. There is a low S-wave velocity zone around 54 m depth, which is indicated by both VSP and Core 26_2 S-wave velocities. The discrepancy in the behavior of the P- and S-wave velocities leads to the unusually low v_p/v_s ratio for the dry core measurements (Figure 8e). Such a low v_p/v_s ratio as well as the large P-wave velocity difference between the dry and saturated cores is indicative of micro cracks (e.g., Liu et al., 1997; Nur & Simmons, 1969; Wang et al., 2012).

5. Interpretation and Discussion of Results

5.1. Structural Interpretation

Borehole 5071_1_B intersects felsic metasediments interlayered with bands of amphibolites at the scale of 1 to 10th of meter, which appears to be consistent with outcrop observations (Rutter et al., 2007). The borehole was intended to be drilled vertically into the hinge zone of the supposedly near-isoclinal Massone antiformal fold structure (Rutter et al., 2007) of which a schematic is shown in Figure 9a. In this regard, the variation of the fracture and foliation dips and their changes with depth are interesting. It is expected that the foliation is steeply

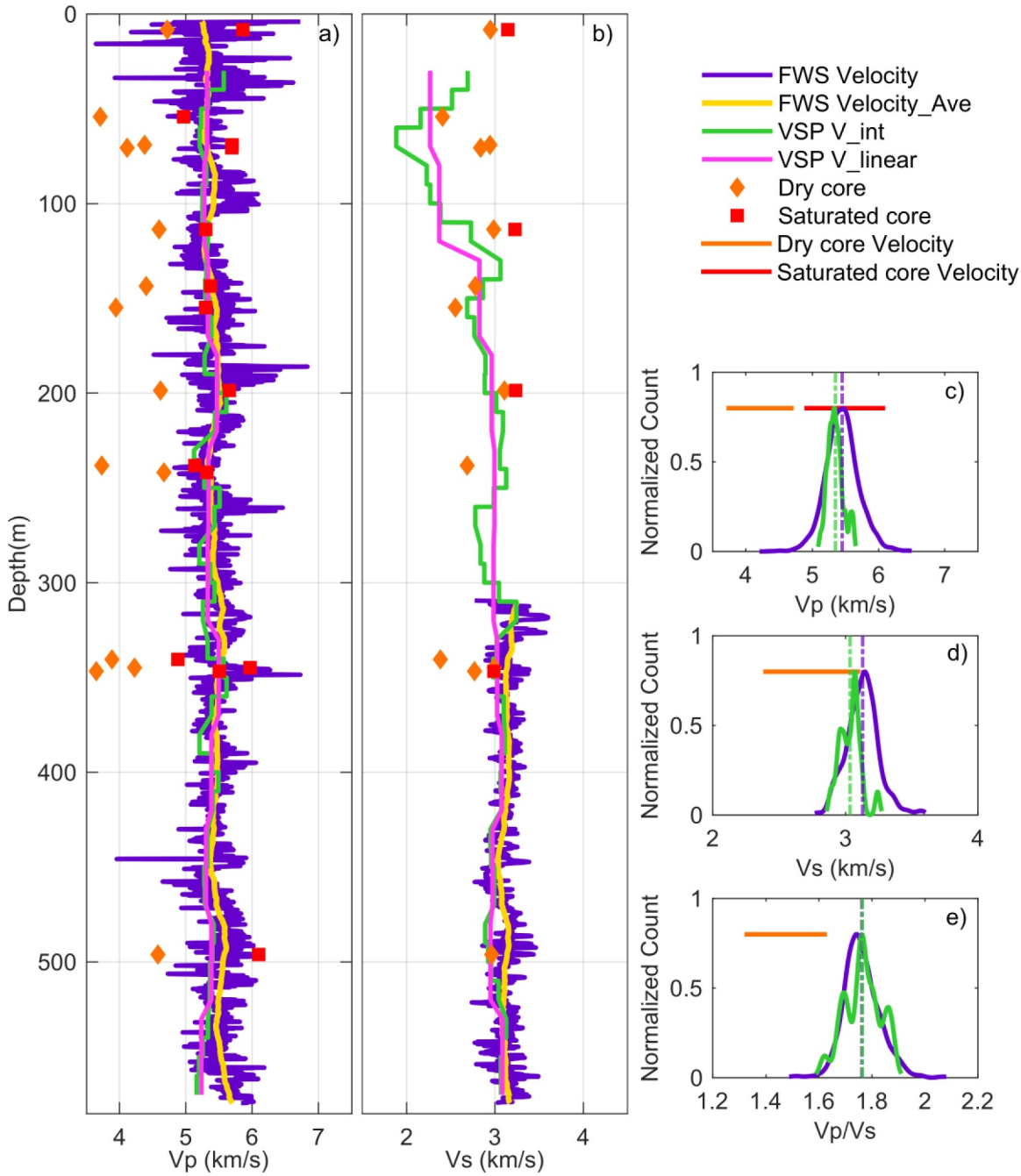

Figure 8. Comparison of (a) P-wave (v_p) and (b) S-wave velocities (v_s) obtained from core, sonic and Vertical seismic profiling data. P-wave (c) and S-wave velocity (d) and v_p/v_s (e) histograms (nonparametric kernel-smoothing distribution) of the sonic and VSP data. Only the S-wave velocities of the HQ section are included. The dashed lines indicate the mean values of the corresponding data and the horizontal lines correspond to the value range of the core measurements.

dipping in the limbs of the antiform as mapped on surface outcrops and less steeply dipping in the center of the hinge zone (Figures 1b and 1c). Foliation dips are measured on core scan photos above 367.8 m and below this depth onsite on cores, whilst fracture orientations are obtained from ATV data. The true orientation of the foliation is not known for the cores and core scans since they have not been oriented. However, in an interval between 330 and 500 m, the quality of the OTV data allows us to identify foliations and correlate them with the core scans. In this interval, the foliation dip azimuths mainly vary between N120° and N160° (SSE to SE) and align with one of the dominant dip azimuths of the fractures as well as the mapped foliation of the southern limb

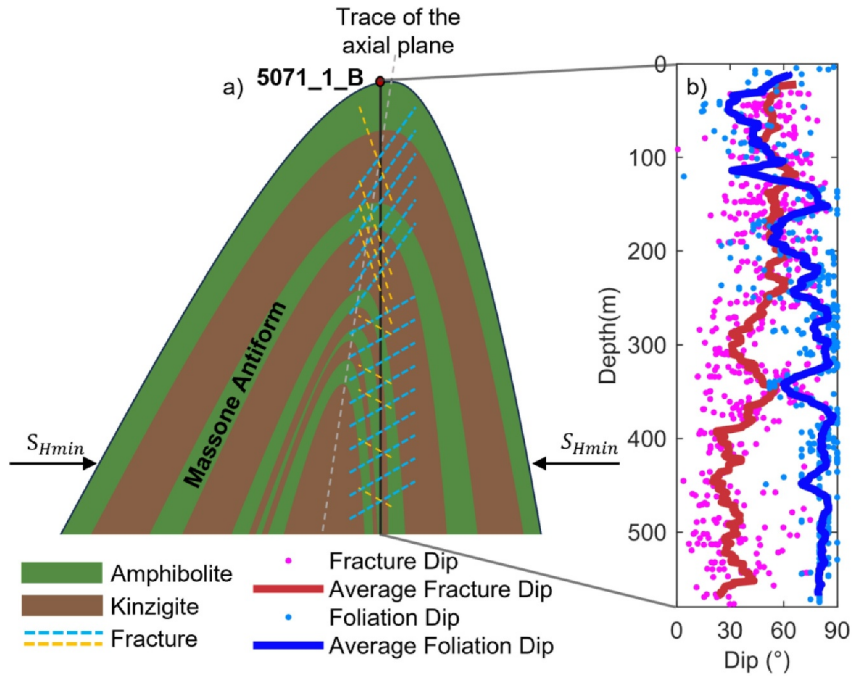

Figure 9. (a) Schematic NW-SE cross-section of the Massone antiform with the borehole track of 5071_1_B. The light blue and yellow dashed lines indicate the fracture dip and dip azimuth corresponding to Figures 4h and 4i. S_{Hmin} indicates the orientation of the minimum horizontal principal stress near the borehole inferred from ATV breakouts. (b) Foliation and fracture dips, inferred from core/core scans and ATV images, respectively.

(Figure 1c). Nevertheless, here we only compare the foliation and fracture dips (Figure 9b), and their spatial 20 m running mean. The foliation dips vary considerably above 230 m depth and then become near vertical from 270 m onwards, except between 325 and 370 m depth, where localized folding might be encountered. Coaxial minor folds are also observed along the Massone antiform (Rutter et al., 2007). Similarly, fracture dips vary above 270 m depth around a mean dip of 54°. Below this depth, a clear trend between fracture and foliation dips occurs with average fracture dips of 37° juxtaposed to the average foliation dips of 80°. This indicates that fractures tend to intersect the foliations at relatively high angles. The dramatic increase in the foliation dip to subvertical as well as the change of the dominant fracture dip possibly controlled by preexisting mechanical anisotropy suggest that at depth 5071_1_B is parallel to one of the limbs of the Massone antiform. Thus, either the Massone antiform is extremely tightly folded and 5071_1_B has not followed the axial plane of the Massone antiform or the axial plane of the Massone antiform is dipping a few degrees west-northwest with the south-eastern limb being quasi vertical as schematically presented in Figure 9a. This is the first local evidence on a 10–100 m scale that the antiform axial plane is tilted, which is not reflected in the structural analysis of Rutter et al. (2007). In their study, a gentle dip to the NE of the axis of the Massone antiform at the northern side of Val d'Ossola is indicated, yet both flanks and the axial plane are vertical. The folding of the Massone antiform and development of the foliation from different deformation phases (likely D1 and D2 of Rutter et al., 2007) are most likely not synchronous with fracture creation, with fractures developing at a later stage. The change in fracture orientation along the borehole may be attributed to either preexisting mechanical anisotropies (change in foliation strength and orientation across the borehole) or a changing stress field at a shallower depth during fracture creation. However, the attribution of fracture development to a specific deformation phase would require a dedicated structural study. The borehole breakouts (Figure 4j) suggest that the present-day maximum horizontal principal stress orientation in the lower section of the borehole is parallel to the fracture planes, allowing them to remain open. However, the in situ inferred stress orientation might be affected by the surrounding high topography as the borehole breakouts are relatively shallow and thus may not present the true stress orientation away from the borehole. Additionally, foliation could further affect the stress orientation estimates from borehole breakouts, as shown in a recent study by Wang et al. (2023).

5.2. Lithological Interpretation of Clustering Results

The cluster analysis yielded distinct clusters for the gamma ray and magnetic susceptibility. These properties are less affected by fractures than the resistivity and velocity logs and are primarily sensitive to the mineralogy of the rock, more precisely, to the radiogenic and magnetic minerals, respectively. The results of the cluster analysis are plotted in Figure 10 as a depth column alongside the core lithologies, which are overlain by the borehole log data and a selection of minerals identified from the core description overlain on the cluster results. The main radiogenic minerals identified in the core description are biotite, muscovite, and K-feldspar (Figure 10f), which is consistent with outcrop data from the Kinzigite formation (e.g., Rutter et al., 2007). Biotite is mapped almost across the entire borehole length, while potassium feldspar and muscovite are only sporadically identified. The accessory phases of the kinzigites include monazite and zircon, which are the main contributors to the U and Th content, respectively, of these rocks. Possible sources of the magnetic susceptibility are sulfides and oxides mapped along the core (Figure 10g). Sulfides are prevalent and occur as part of the matrix being barely visible, as large sulfides in leucosomes, as large crystals within leucocratic veins of metamafic enclaves in the kinzigites and along some fractures. These core observations may provide some insights into the discrepancy between the main lithologies and the identified three clusters as well as shed light on the differences between the clusters. In general, there is a notable spatial variability in this continuous section of lower crustal rocks. Nevertheless, the amphibolites combined with the calcsilicates and cluster 2 as well as the kinzigites and clusters 1 and 3 show a very good agreement below 105 m depth. In general, the amphibolites and calcsilicates correlate with the identified amphiboles in the core description. Between 19 and 39 m, 122 and 126 m as well as 185 and 196 m depth the data points in cluster 2 correspond to the calcsilicates with low gamma ray and high magnetic susceptibility accounting for 7.32% of total data points. In the section of 53–94 m depth, calcsilicates, kinzigites and amphibolites are thinly interlayered. The cluster analysis also predicts an interlayered sequence of the three clusters. Nevertheless, calcsilicates in this section, accounting for 1.92% of all data points and some amphibolites above 19 m, accounting for 3%, have relatively high gamma ray and high magnetic susceptibility values, and are consequently grouped into cluster 1.

Cluster 3, corresponding to the low gamma ray and low magnetic susceptibility kinzigites, mainly occurs at the depth intervals of 104–177 m and 265–310 m. In these sections most of the leucosomes occur, especially between 105 and 116 m, while they are less common in cluster 1 (Figure 10g). Interestingly, in the same section sulfides are not identified in the core description, which may contribute to the lower susceptibilities. The significant difference in natural gamma radiation between the two clusters cannot be directly explained by the visual core observations. It is expected that the kinzigites are enriched in radioactive elements (e.g., Redler et al., 2012); thus, the low radioactivity of cluster 3 is somewhat surprising. This may be due to variable volume fractions and/or different potassium-rich minerals and/or the absence of uranium- and thorium-rich minerals in kinzigites of cluster 3. A variation in K, U, and Th content may reflect differences in the composition of the source rocks (e.g., quartz-rich or clay rich sediments) preserved during metamorphism. To further investigate the origin of these two distinct groups of kinzigites dedicated petrology focused studies and detailed mineralogical laboratory analysis are planned and ongoing. Overall, the magnetic susceptibility values fall into the low susceptibility range, with a few metamafics falling between the low and intermediate ranges defined by Belluso et al. (1990). This may cause local (short wavelength) magnetic anomalies measured near the surface. The magnitude of magnetic susceptibility correlates with lithotypes but is spatially quite variable within them, which corroborates previous findings for the Kinzigite formation (e.g., Belluso et al., 1990).

The fuzzy areas generally correspond to lithology boundaries or transition zones. Even though no lithological impact on the P-wave velocity can be inferred from the crossplots and boxplots, it can be observed that for some amphibolite layers below 150 m depth, the P-wave velocity is higher than for the neighboring felsic metasediments denoted by black arrows in Figure 10c.

5.3. Implications of Velocity and Density Variations in 5071_1_B for Seismic Reflections

Seismic reflectivity is governed by impedance contrasts due to velocity and/or density contrasts at frequencies compatible with the seismic survey. Despite the occurrence of numerous lithological changes along the borehole track, the velocities in borehole 5071_1_B do not exhibit a systematic correlation with the main lithologies nor with the identified clusters. This is in contrast to the velocities reported for outcrop samples in the IVZ. Several laboratory measurements have been conducted to constrain the velocities and densities of different lithologies in

10.1029/2024GC011707

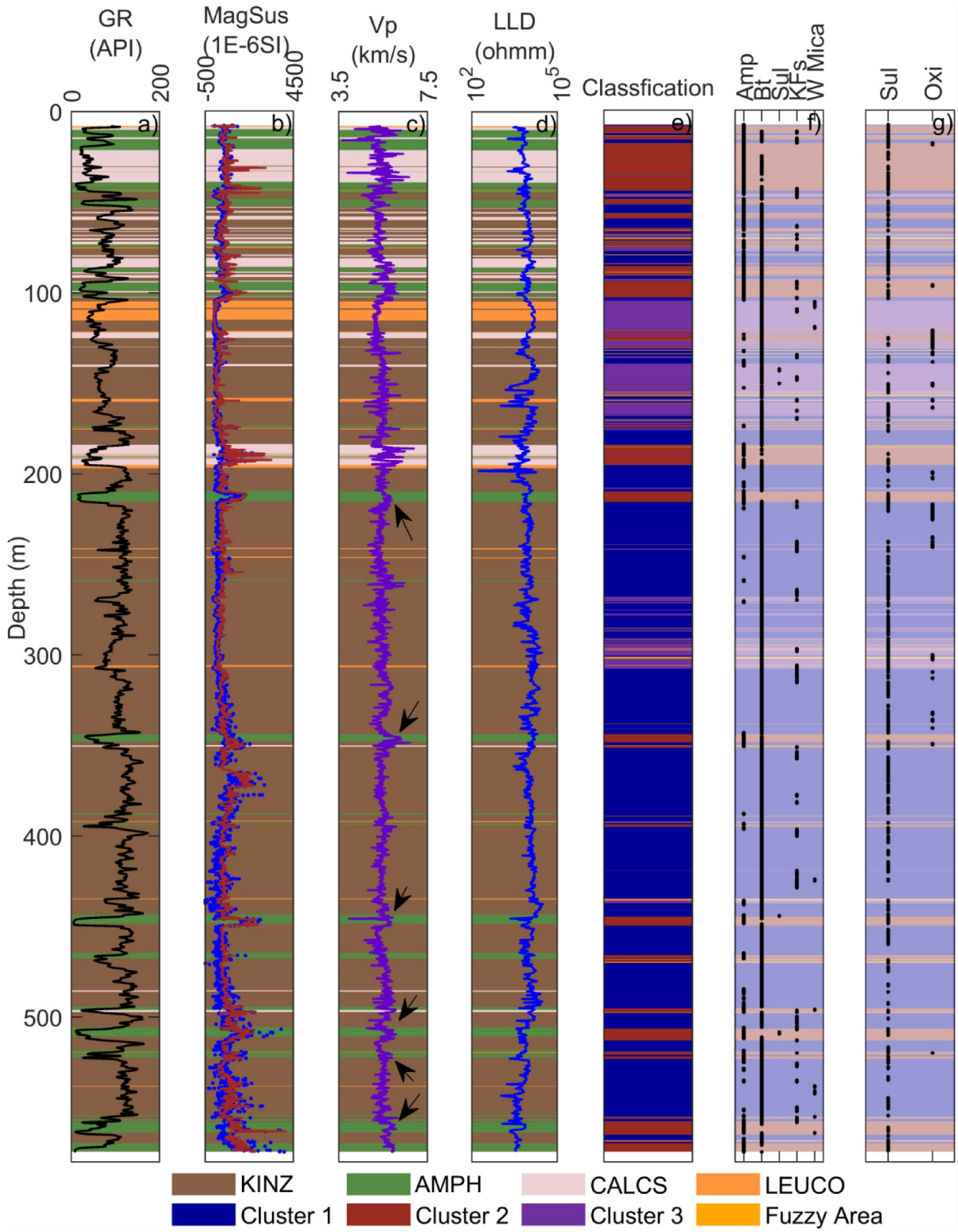

Figure 10. Borehole log data overlain on core lithologies: (a) gamma ray (GR), (b) magnetic susceptibility (MagSus, the red line denotes the log data and the blue dots the core data), (c) sonic P-wave velocity (Vp), black arrows indicate local high velocity sections, (d) deep laterolog resistivity (LLD) and (e) depth column of the cluster results. Visual onsite core observations (f) of amphibole (Amp), biotite (Bt), sulfide (Sul), potassium feldspar (KFs), white mica (W Mica), classified as major minerals and (g) of sulfide (Sul) and oxide (Oxi), which are classified as minor minerals as well as the intervals containing leucosome (Leuc), overlain on the cluster results.

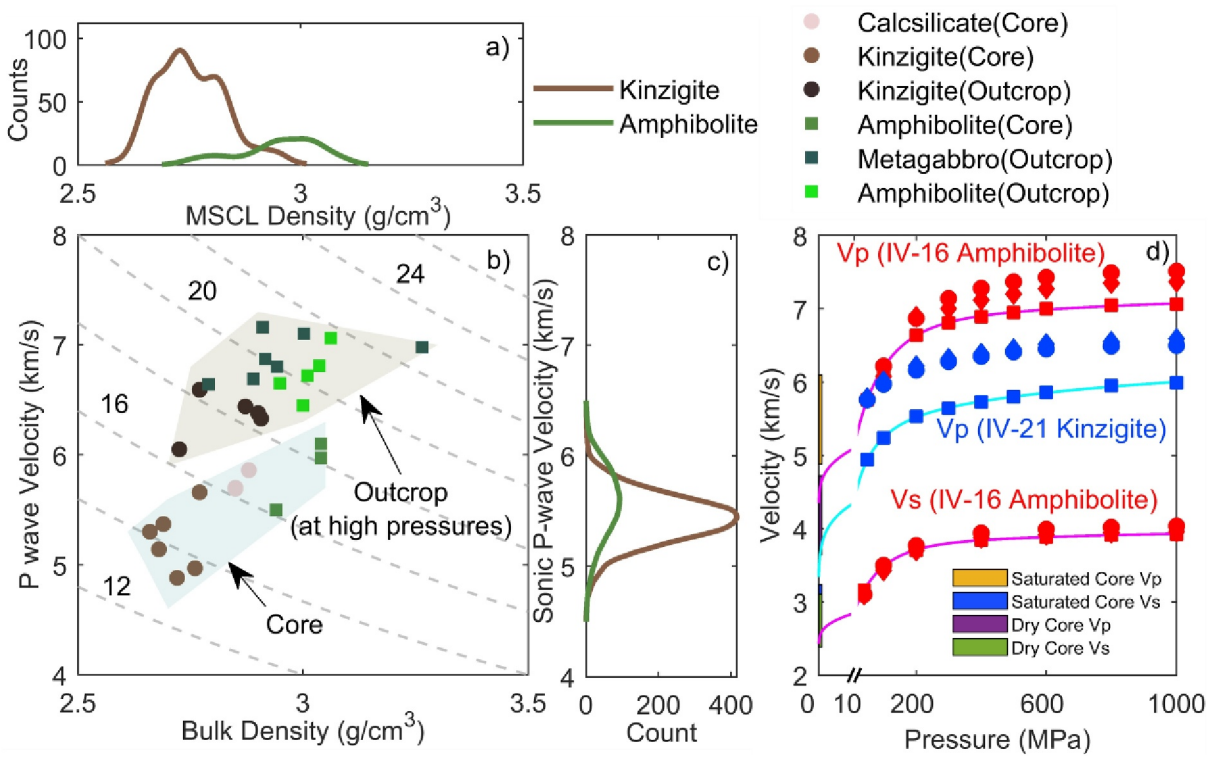

Figure 11. Comparison of velocity and density data of 5071_1_B with literature data. (a) multi-sensor core logger density histograms (nonparametric kernel-smoothing distribution) of kinzigites and amphibolites of 96 core sections in borehole 5071_1_B. (b) P-wave velocity and bulk density of 5071_1_B saturated core samples and outcrop samples at high pressures (Burke & Fountain, 1990). The dashed gray isolines represent values of constant acoustic impedance (unit: km/s*g/cm^3). (c) Sonic P-wave velocity histograms (nonparametric kernel-smoothing distribution) of kinzigites and amphibolites. (d) Velocity as function of confining pressure for an amphibolite (v_p from Burke & Fountain, 1990; v_s from Fountain, 1976) and a kinzigite (Kinzigite formation) core sample (from Burke & Fountain, 1990) near 5071_1_B. Velocities are shown along three structural directions: dots–parallel to the lineation, diamonds–perpendicular to the lineation and squares–normal to the foliation. The solid lines denote the fitted relationship according to Wepfer and Christensen (1991). The rectangles indicate the velocities of the 15 5071_1_B core samples under ambient conditions.

the IVZ (Barberini et al., 2007; Belluso et al., 1990; Biedermann et al., 2020; Khazanehdari et al., 2000; Musacchio et al., 1998). In these studies, the velocities are commonly measured up to in situ pressures, which are typical for the lower crust at great depth.

A selection of published high-pressure intrinsic P-wave velocities and bulk densities of outcrop samples (Burke & Fountain, 1990; Fountain, 1976) are shown in Figure 11b and compared to the P-wave velocities and bulk densities of the 15 5071_1_B cores. Additionally, the MSCL density and sonic velocities of 5071_1_B for two of the main lithologies are displayed in Figures 11a and 11c. The outcrop samples and 5071_1_B cores with higher densities tend to have higher velocities and display a lithology trend. The densities of the outcrop and 5071_1_B samples are consistent. They fall within the range of 2.6–2.9 g/cm^3 for kinzigites and within 2.9–3.1 g/cm^3 for amphibolite rocks. The high-pressure P-wave velocities of 6–7.5 km/s for the outcrop samples are significantly higher than those measured for the 5071_1_B cores at ambient conditions and the sonic logging velocities (Figure 11c). The reason is the strong pressure dependence of the rocks due to microcracks. An example of the ultrasonic velocity pressure relationship for a dry metasediment of the Kinzigite formation (plagioclase-biotite-quartz gneiss) and a dry amphibolite from Fountain (1976) and Burke and Fountain (1990) near the drilling site of 5071_1_B is shown in Figure 11d. These pressure-dependent velocities are extrapolated to an ambient pressure of 0.1 MPa using the equation proposed by Wepfer and Christensen (1991). The extrapolated velocities fall into the same velocity range as the those of the 15 dry 5071_1_B core samples (Figure 11d). This supports the interpretation that the low 5071_1_B core velocities can be attributed to microcracks.

To further corroborate this interpretation, we model the influence of dry and saturated cracks on ultrasonic velocities using Hudson's model for an orthogonal set of cracks (Mavko et al., 2009). As input for the intact rock

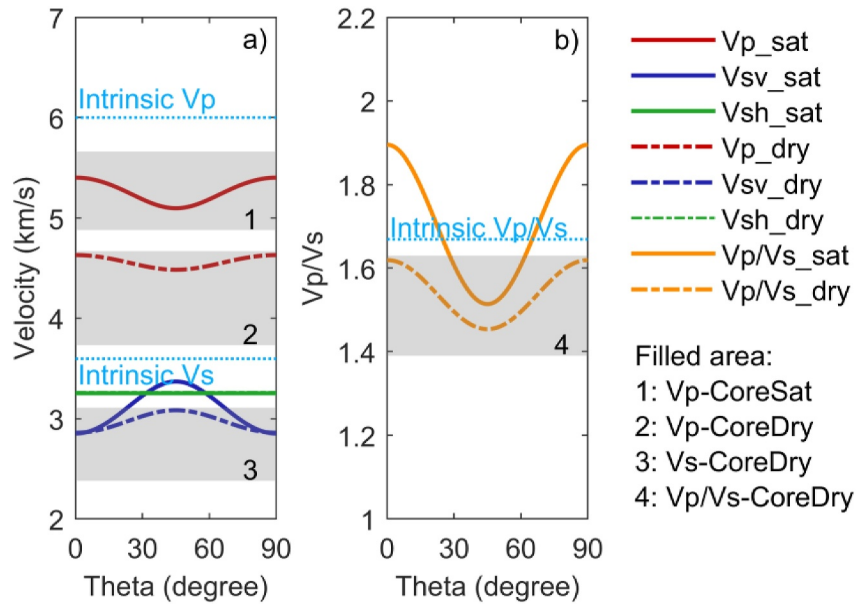

Figure 12. Comparison of modeling results (red, blue, green and yellow lines) using the second order correction of Hudson's model (crack density is 0.09) with core data (Mavko et al., 2009). Velocity (a) and v_p/v_s (b) as function of the crack set orientation angle with respect to the incident wave. The gray boxes denote the velocity ranges of the kinzigites of 5071_1_B. Intrinsic velocities (light blue dotted lines) of an outcrop metapelite (IV-76) from Burlini and Fountain (1993) were extrapolated to zero-pressure velocities.

velocities, intrinsic velocities at which all cracks are closed of an outcrop metapelite (IV-76) sample from Burlini and Fountain (1993) are utilized. Figure 12 shows the intrinsic velocities and corresponding v_p/v_s, the calculated velocities and v_p/v_s from Hudson's model, as well as the velocity and v_p/v_s range of the 5071_1_B kinzigite core measurements. The calculated velocities are shown as a function of the crack set orientation with respect to the propagation direction of the ultrasonic wave. For orientations of the crack set between 0°-25° (75°–90°), Hudson's model offers a potential explanation of the measured velocities and v_p/v_s of the core data. The v_p/v_s values are governed by microcracks and depend on their orientation with respect to the ray path (Wang et al., 2012). They are not representative of crack free rocks of the lower crust, for which the v_p/v_s will be governed by the mineralogical composition. The orthogonal crack set used here may not be a realistic model. More probable scenarios include a preferred orientation of cracks with respect to the rock microstructure or the stress field around the borehole (Dresen & Guéguen, 2004; Nur & Simmons, 1969). The latter is observed for the conjugate fracture set in the ATV data. To further constrain the orientation and distribution of microcracks, additional measurements on oriented core samples are necessary. Nevertheless, the simple model confirms that cracks are the likely cause of the velocity behavior at the core scale. Commonly, microcracks in drill cores are attributed to depressurization and anisotropic stress relaxation of the drilled core material (e.g., Kästner et al., 2021; Wolter & Berckhemer, 1989; Zang et al., 1989). However, the fact that the velocities across all three scales (core, sonic and VSP) are generally consistent suggests that microcracks also affect the sonic and VSP velocities. The horizontal resolution of P-waves, as defined by the Fresnel zone width, falls between 0.7 and 1 m for the sonic data and 45–340 m for the VSP data. This suggests that micro-cracks exist in situ away from the immediate vicinity of the borehole. This is plausible given that 5071_1_B is drilled into a deformation structure and is only 578.5 m deep. The effective vertical pressure (lithostatic pressure—pore pressure) ranges from 0.26 MPa near the top of the borehole to 9.86 MPa at the bottom of the borehole, falling into the non-linear part of the velocity pressure curve. Consequently, along the borehole, the lithostatic pressure would be insufficient to close existing microcracks. Furthermore, the average P-wave velocity difference for dry and saturated amphibolite cores is around 1.71 km/s and higher than the average difference of 1.17 km/s for kinzigite cores, suggesting that amphibolites are more micro-cracked. This in-turn may partly explain the similar P-wave velocities observed for kinzigites and amphibolites along the borehole. This may also explain the slightly higher resistivities in the kinzigites compared to the amphibolites.

Thus, reflections due to lithological velocity contrasts are not very likely in 5071_1_B. However, lithological reflections may occur due to the density contrast between kinzigites and amphibolites (Figure 11a) observed for the MSCL and core density measurements, resulting in acoustic impedance contrasts between the two main lithologies indicated by isolines. The acoustic impedance contrasts are of a similar magnitude as reported for the laboratory data of Barberini et al. (2007). The velocities in 5071_1_B are not only affected by micro-cracks but also by fractures. Therefore, low seismic velocities in this borehole are likely to be governed by brittle deformation at various scales. Seismic reflections might be caused by large-scale fractures. For example, a distinct fracture identified by the ATV data at 445.6 m decreases the sonic P-wave velocity to 3.95 km/s in Figure 10a, which is significantly lower than the velocity (above 5 km/s) of the surrounding rock mass.

Another factor which influences velocity is seismic anisotropy. Both amphibolites and kinzigites in Figure 11d show an anisotropic velocity behavior. 5071_1_B is drilled into the top of the Massone antiform and the foliation dip angle varies between 30° and 60° in the upper part of the borehole and becomes increasingly steeper in the deeper part (Figure 9a). In general, a seismic wave propagating perpendicular to the rock foliation has the lowest velocity compared to the other directions. In Figure 8a, it can be observed that the sonic P-wave velocity slightly increases with depth below 450 m. This may be caused by the steeply dipping foliation, which counteracts the effect of fractures (and micro-cracks) on the sonic velocities. The sonic velocity trend cannot be observed in the VSP P-wave velocity, which may be more impacted by the large-scale fractures. More detailed modeling is necessary to distinguish the combined effects of foliation, micro-cracks and fractures on the VSP data of 5071_1_B, which is outside the scope of this paper. Nevertheless, the data clearly indicates that the velocities are primarily impacted by structural factors and only locally correlate with the lithology. An additional factor which may contribute to a low v_p/v_s ratio is the intrinsic anisotropy of rocks, for example, caused by foliation.

6. Conclusions

In order to structurally and lithologically characterize the upper part of the lower continental crust in the IVZ, we have carried out an integrated analysis of core and borehole geophysical data collected in borehole 5071_1_B. The borehole was designed to be drilled vertically into the hinge zone of the tightly folded Massone antiform. However, the structural data, fracture and foliation dips, indicate that the borehole started in the hinge zone and was then drilled sub-parallel to the limb, suggesting that the axis of the antiform dips a few degrees to the west-northwest at this location. Numerous natural planar fractures have been identified with two dominant dip azimuthal orientations: NW to NE and SSE to SE. Borehole breakouts in the lower part of the borehole indicate that the present-day maximum horizontal principal stress orientation is parallel to the fracture planes, thereby keeping them open. These open fractures correlate with an abundance of anomalies in the electrical logs and sonic velocities. A correlation between core lithologies is not evident in the resistivity data and can only be observed locally for the sonic velocities. Consequently, the lithological rock mass characterization is based on the gamma ray and magnetic susceptibility logs using fuzzy c-means clustering. The clustering results show an excellent agreement with the lithological core description in the presence of a remarkable spatial variability of this continuous sample of lower crust. Furthermore, the cluster analysis revealed two distinct groups of kinzigites, one characterized by high magnetic susceptibility and gamma radiation and the other by low magnetic susceptibility and gamma radiation. In particular, the low gamma ray values are surprising as the kinzigites are expected to be enriched in radioactive elements. Despite the numerous lithological changes along the borehole track, seismic reflections due to lithological velocity contrasts are not expected in the vicinity of 5071_1_B, but reflectivity due to density contrasts may be possible. Velocities in 5071_1_B fall between 5 and 6 km/s for P-waves and are around 3 km/s for S-waves on all three scales, that is, core, sonic and VSP. These rather low velocities for lower crustal rocks are characteristic of microcracked rocks at low pressures. Micro-cracks are suspected to be open under the in situ stress conditions of 5071_1_B. As a result, the velocities are controlled by the brittle deformations at different scales in the borehole and not by lithological changes. The study highlights the importance of considering the effects of fractures at multiple scales, when folded structures such as the Massone antiform become brittle when they are exhumed and cooled. The stress conditions and open and compliant fractures and fracture zones, which may be inherited from the geological history of the rocks, will also affect the reflectivity in the encountered rock mass.

Appendix A: MSCL Density Correction

Generally, an empirical method is utilized for the bulk density calibration (GEOTEK, 2021). Since the calibration with a dedicated calibration piece was not successfully performed, we use densities of 15 core samples for calibration, which are measrued using Archimedes' principle. A total of 96 core sections were scanned with a 2 cm spatial interval using the MSCL before cutting the core samples. Due to the 15 whole round samples being approximately 10 cm in length, we take the average values of 5 intensity points corresponding to the depth section of the corresponding core sample after removing the outliers. The empirical equation is written as follows:

$$ln(\text{Intensity}) = A * (D * \rho)^2 + B * (D * \rho) + C,$$

where ρ is the core density in g/cm^3, D is the core diameter in cm, Intensity is the measured intensity in cps and A, B, C are calibration coefficients.

Figure A1a shows the second-order polynomial regression for core sample data. This relationship is used for calibrating the intensities of 96 core sections. The calibrated densities are shown in Figure A1b.

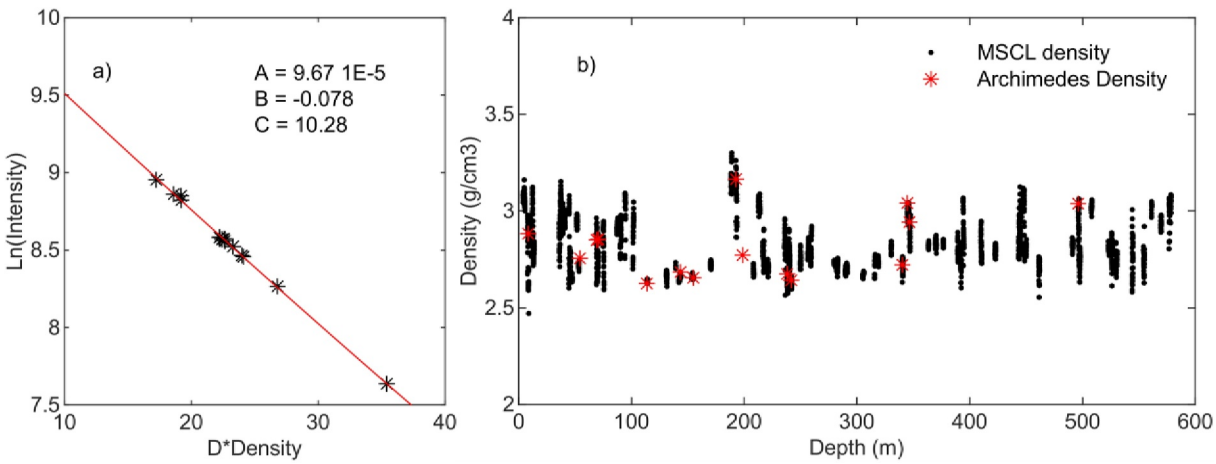

Figure A1. Density calibration: (a) Calibration curve for 15 core samples and (b) calibrated multi-sensor core logger densities for 96 selected core sections along the borehole DT-1B. The red asterixis denote the core density measurement using Archimedes' principle.

Appendix B: Core Measurements

Table B1
Summarizes the Results of the Velocity and Density Measurements Under Ambient Conditions for the 15 Whole Round Core Samples

Core #	Depth* (m)	ρ ** (g/cm^3)	Vp_Dry (m/s)	Vp_Sat (m/s)	Vs_Dry (m/s)	Vs_Sat (m/s)	Vp/Vs (dry)	Vp/Vs (Sat)	Lithology
006_1	8.10	2.88	4.72	5.86	2.95	3.15	1.60	1.86	Calcsilicate
026_2	54.03	2.76	3.71	4.97	2.41	–	1.54	–	Kinzigite
031_1	68.85	2.85	4.38	5.70	2.94	–	1.49	–	Calcsilicate
031_3	70.38	2.85	4.11	5.69	2.84	–	1.45	–	Calcsilicate
048_3	113.44	2.63	4.60	5.30	2.99	3.23	1.54	1.64	Leucosome
058_2	143.30	2.69	4.40	5.37	2.78	–	1.58	–	Kinzigite
064_1	154.65	2.66	3.94	5.30	2.55	–	1.55	–	Kinzigite
083_1	192.50	3.16	–	–	–	–	–	–	Calcsilicate
085_1	198.39	2.77	4.62	5.66	3.11	3.23	1.49	1.75	Kinzigite
099_2	237.96	2.68	3.73	5.14	2.69	–	1.39	–	Kinzigite

Table B1
Continued

Core #	Depth* (m)	ρ ** (g/cm^3)	Vp_Dry (m/s)	Vp_Sat (m/s)	Vs_Dry (m/s)	Vs_Sat (m/s)	Vp/Vs (dry)	Vp/Vs (Sat)	Lithology
100_2	241.57	2.64	4.67	5.32	–	–		–	Leucosome
135_2	340.21	2.72	3.88	4.88	2.38	–	1.63	–	Kinzigite
137_3	344.57	3.04	4.22	5.97	2.99	–	1.41	–	Amphibolite
138_1	346.45	2.94	3.65	5.50	2.77	2.99	1.32	1.84	Amphibolite
193R_2	495.85	3.04	4.58	6.10	2.96	–	1.54	–	Amphibolite

Note. *Depth: geologist's depth of the sample intermediate point, **ρ: bulk density determined with the Archimedes' method.

Data Availability Statement

Data used in this study have been collected in the framework of the ICDP DIVE project, with an inherent moratorium until June 2026. The VSP velocities, well logging and MSCL data used in the study will be publicly available from the GFZ data Services (Li et al., 2024) after the DIVE moratorium period.

Acknowledgments
This research and the PhD position of Junjian Li is funded by the Austrian Science Fund (FWF) (Grant DOI: 10.55776/P35102). This research used data from the DIVE drilling project funded by: the International Continental Scientific Drilling Program (ICDP) with expedition ID 5071 (lead PIs: O. Müntener, M. Pistone, L. Ziberna, G. Hetényi, A. Zanetti, A. Greenwood, D. Giovannelli), the Swiss National Science Foundation (SNF Grant 200021-204491, PIs: O. Müntener, J. Hermann, G. Hetényi, K. Holliger, D. Rubatto), the Austrian Science Fund (FWF Project: P 35102-N, PI: A. Greenwood), the German Science Foundation (DFG: TO901/1-1, PI: V. Toy), the French National Research Agency (Grant Agreement No. ANR-20-CE01-0200), the Institut Universitaire de France (research fellowship to L. Truche), the Italian CNR (PNRR-ITINERIS: IR0000032; PNRR-MEET: IR0000025) and INGV (Progetto DIVE@INGV and Project INGV Pianeta Dinamico 2023–2025, Theme MT_UNLOCK, Grant CUP D53J19000170001, supported by the Italian Ministry of University and Research), the Swiss Geophysical Commission, and multiple contributions from the University of Lausanne. Partial support to D. Giovannelli via funding from the European Research Council (ERC) under the European Union's Horizon 2020 research and innovation program (Grant Agreement No. 948972—COEVOLVE—ERC-2020-STG). We would also like to thank the DIVE scientist team for their contribution to this research.

References

Abdi, H., & Williams, L. J. (2010). Principal component analysis. *WIREs Computational Statistics*, *2*(4), 433–459. https://doi.org/10.1002/wics.101

Avseth, P., Mukerji, T., & Mavko, G. (2005). *Quantitative seismic interpretation: Applying rock physics tools to reduce interpretation risk* (1st ed.). Cambridge University Press. https://doi.org/10.1017/CBO9780511600074

Barberini, V., Burlini, L., & Zappone, A. (2007). Elastic properties, fabric and seismic anisotropy of amphibolites and their contribution to the lower crust reflectivity. *Tectonophysics*, *445*(3–4), 227–244. https://doi.org/10.1016/j.tecto.2007.08.017

Barboza, S. A., Bergantz, G. W., & Brown, M. (1999). Regional granulite facies metamorphism in the Ivrea zone: Is the Mafic complex the smoking gun or a red herring? *Geology*, *27*(5), 447. https://doi.org/10.1130/0091-7613(1999)027<0447:RGFMIT>2.3.CO;2

Barruol, G., & Kern, H. (1996). Seismic anisotropy and shear-wave splitting in lower-crustal and upper-mantle rocks from the Ivrea zone—Experimental and calculated data. *Physics of the Earth and Planetary Interiors*, *95*(3–4), 175–194. https://doi.org/10.1016/0031-9201(95)03124-3

Barton, C. A., Zoback, M. D., & Burns, K. L. (1988). In-situ stress orientation and magnitude at the Fenton Geothermal Site, New Mexico, determined from wellbore breakouts. *Geophysical Research Letters*, *15*(5), 467–470. https://doi.org/10.1029/GL015i005p00467

Barton, N., & Stephansson, O. (1990). *Rock joints: Proceedings of a regional conference of the international society for rock mechanics, Loen, 4-6 June 1990*. CRC Press.

Bea, F., & Montero, P. (1999). Behavior of accessory phases and redistribution of Zr, REE, Y, Th, and U during metamorphism and partial melting of metapelites in the lower crust: An example from the Kinzigite Formation of Ivrea-Verbano, NW Italy. *Geochimica et Cosmochimica Acta*, *63*(7), 1133–1153. https://doi.org/10.1016/S0016-7037(98)00292-0

Bell, J. S., & Gough, D. I. (1979). Northeast-southwest compressive stress in Alberta evidence from oil wells. *Earth and Planetary Science Letters*, *45*(2), 475–482. https://doi.org/10.1016/0012-821X(79)90146-8

Belluso, E., Biino, G., & Lanza, R. (1990). New data on the rock magnetism in the Ivrea-Verbano Zone (Northern Italy) and its relationships to the magnetic anomalies. *Tectonophysics*, *182*(1), 79–89. https://doi.org/10.1016/0040-1951(90)90343-7

Berckhemer, H. (1969). Direct evidence for the composition of the lower crust and the Moho. *Tectonophysics*, *8*(2), 97–105. https://doi.org/10.1016/0040-1951(69)90083-3

Bezdek, J. C., Ehrlich, R., & Full, W. (1984). FCM: The fuzzy *c*-means clustering algorithm. *Computers & Geosciences*, *10*(2), 191–203. https://doi.org/10.1016/0098-3004(84)90020-7

Biedermann, A. R., Kunze, K., & Zappone, A. S. (2020). Crystallographic preferred orientation, magnetic and seismic anisotropy in rocks from the Finero peridotite, Ivrea-Verbano Zone, Northern Italy – Interplay of anisotropy contributions from different minerals. *Tectonophysics*, *782–783*, 228424. https://doi.org/10.1016/j.tecto.2020.228424

Bloomer, S. F., & Mayer, L. A. (1997). Core-log-seismic integration as a framework for determining the basin-wide significance of regional reflectors in the eastern equatorial Pacific. *Geophysical Research Letters*, *24*(3), 321–324. https://doi.org/10.1029/96GL02076

Brack, P., Ulmer, P., & Schmid, S. M. (2010). A crustal-scale magmatic system from the Earth's mantle to the Permian surface—Field trip to the area of lower Valsesia and Val d'Ossola (Massiccio dei Laghi, Southern Alps, Northern Italy). *Swiss Bulletin for Applied Geology*, *15*, 3–21.

Brodie, K. H., & Rutter, E. H. (1987). Deep crustal extensional faulting in the Ivrea zone of northern Italy. *Tectonophysics*, *140*(2), 193–212. https://doi.org/10.1016/0040-1951(87)90229-0

Burke, M. M., & Fountain, D. M. (1990). Seismic properties of rocks from an exposure of extended continental crust—New laboratory measurements from the Ivrea zone. *Tectonophysics*, *182*(1–2), 119–146. https://doi.org/10.1016/0040-1951(90)90346-A

Burlini, L. (2008). *Parco Nazionale della Val Grande: Carta Geologica (1:25'000)*. ETH Zürich.

Burlini, L., & Fountain, D. M. (1993). Seismic anisotropy of metapelites from the Ivrea-Verbano zone and Serie dei Laghi (northern Italy). *Physics of the Earth and Planetary Interiors*, *78*(3–4), 301–317. https://doi.org/10.1016/0031-9201(93)90162-3

Caspari, E., Greenwood, A., Baron, L., Egli, D., Toschini, E., Hu, K., & Holliger, K. (2020). Characteristics of a fracture network surrounding a hydrothermally altered shear zone from geophysical borehole logs. *Solid Earth*, *11*(3), 829–854. https://doi.org/10.5194/se-11-829-2020

Chroston, P. N., & Simmons, G. (1989). Seismic velocities from the Kohistan volcanic arc, northern Pakistan. *Journal of the Geological Society*, *146*(6), 971–979. https://doi.org/10.1144/gsjgs.146.6.0971

Decarlis, A., Zanetti, A., Ogunyele, A. C., Ceriani, A., & Tribuzio, R. (2023). The Ivrea-Verbano tectonic evolution: The role of the crust-mantle interactions in rifting localization. *Earth-Science Reviews*, *238*, 104318. https://doi.org/10.1016/j.earscirev.2023.104318

Diehl, T., Husen, S., Kissling, E., & Deichmann, N. (2009). High-resolution 3-D P-wave model of the Alpine crust. *Geophysical Journal International*, *179*(2), 1133–1147. https://doi.org/10.1111/j.1365-246X.2009.04331.x

Dresen, G., & Guéguen, Y. (2004). Damage and rock physical properties. *International Geophysics Series*, *89*, 169–218.

Elger, J., Berndt, C., Kästner, F., Pierdominici, S., Kück, J., Almqvist, B. S. G., et al. (2021). Core-log-seismic integration in metamorphic rocks and its implication for the regional geology: A case study for the ICDP drilling project COSC-1, Sweden. *Geochemistry, Geophysics, Geosystems*, *22*(3), e2020GC009376. https://doi.org/10.1029/2020GC009376

Ellis, D. V. & Singer, J. M. (Eds.). (2007). *Well logging for Earth scientists*. Springer. https://doi.org/10.1007/978-1-4020-4602-5

Emmermann, R., & Lauterjung, J. (1997). The German continental deep drilling program KTB: Overview and major results. *Journal of Geophysical Research*, *102*(B8), 18179–18201. https://doi.org/10.1029/96JB03945

Ewing, T. A., Hermann, J., & Rubatto, D. (2013). The robustness of the Zr-in-rutile and Ti-in-zircon thermometers during high-temperature metamorphism (Ivrea-Verbano Zone, northern Italy). *Contributions to Mineralogy and Petrology*, *165*(4), 757–779. https://doi.org/10.1007/s00410-012-0834-5

Fountain, D. M. (1976). The Ivrea—Verbano and Strona-Ceneri zones, northern Italy: A cross-section of the continental crust—New evidence from seismic velocities of rock samples. *Tectonophysics*, *33*(1–2), 145–165. https://doi.org/10.1016/0040-1951(76)90054-8

Fountain, D. M. (1989). Growth and modification of lower continental crust in extended terrains: The role of extension and magmatic underplating. In *Properties and processes of Earth's lower crust* (pp. 287–299). American Geophysical Union (AGU). https://doi.org/10.1029/GM051p0287

GEOTEK. (2021). Multi-sensor core logger – Standard manual.

Goff, J. A., & Holliger, K. (2003). Heterogeneity in the crust and upper mantle: Nature, scaling, and seismic properties. *Springer Science & Business Media*, 67–94. https://doi.org/10.1007/978-1-4615-0103-9

Hale, L. D., & Thompson, G. A. (1982). The seismic reflection character of the continental Mohorovicic discontinuity. *Journal of Geophysical Research*, *87*(B6), 4625–4635. https://doi.org/10.1029/JB087iB06p04625

Handy, M. R. (1987). The structure, age and kinematics of the Pogallo fault zone; southern alps, northwestern Italy. *Eclogae Geologicae Helvetiae*, *80*(3), 593–632.

Hearst, J. (2000). *Well logging for physical properties: A handbook for geophysicists, geologists, and engineers* (2nd ed.). John Wiley Publishing. Retrieved from https://www.biblio.com/book/well-logging-physical-properties-handbook-geophysicists/d/1261868445

Henk, A., Franz, L., Teufel, S., & Oncken, O. (1997). Magmatic underplating, extension, and crustal reequilibration: Insights from a cross-section through the Ivrea zone and Strona-Ceneri zone, northern Italy. *The Journal of Geology*, *105*(3), 367–378. https://doi.org/10.1086/515932

Kästner, F., Pierdominici, S., Elger, J., Zappone, A., Kück, J., & Berndt, C. (2020). Correlation of core and downhole seismic velocities in high-pressure metamorphic rocks: A case study for the COSC-1 borehole, Sweden. *Solid Earth*, *11*(2), 607–626. https://doi.org/10.5194/se-11-607-2020

Kästner, F., Pierdominici, S., Zappone, A., Morales, L. F. G., Schleicher, A. M., Wilke, F. D. H., & Berndt, C. (2021). Cross-scale seismic anisotropy analysis in metamorphic rocks from the COSC-1 borehole in the Scandinavian Caledonides. *Journal of Geophysical Research: Solid Earth*, *126*(5), e2020JB021154. https://doi.org/10.1029/2020JB021154

Kaufman, L., & Rousseeuw, P. J. (2009). *Finding groups in data: An introduction to cluster analysis*. John Wiley & Sons.

Kern, H., & Schenk, V. (1985). Elastic wave velocities in rocks from a lower crustal section in southern Calabria (Italy). *Physics of the Earth and Planetary Interiors*, *40*(3), 147–160. https://doi.org/10.1016/0031-9201(85)90126-8

Khazanehdari, J., Rutter, E. H., & Brodie, K. H. (2000). High-pressure-high-temperature seismic velocity structure of the midcrustal and lower crustal rocks of the Ivrea-Verbano zone and Serie dei Laghi, NW Italy. *Journal of Geophysical Research*, *105*(B6), 13843–13858. https://doi.org/10.1029/2000JB900025

Kissling, E. (1984). Three dimensional gravity model of the northern Ivrea-Verbano zone. In J. J. Wagner & S. Mueller (Eds.), *Geomagnetic and gravimetric studies of the Ivrea zone* (pp. 53–61). Swiss Geophysical Commission, Kümmerly & Frey.

Kitzig, M. C. (2018). Integration of geochemical and geophysical data for downhole rock mass characterisation (Doctoral dissertation, Curtin University). https://espace.curtin.edu.au/handle/20.500.11937/68385

Kozlovsky, Y. A., & Adrianov, N. I. (Eds.). (1987). *The superdeep well of the Kola Peninsula* (p. 557). Springer.

Lanza, R. (1982). Models for interpretation of the magnetic anomaly of the Ivrea body. *Geologie Alpine*, *58*, 85–94.

Li, J., Caspari, E., Greenwood, A., Pierdominici, S., Baron, L., Kück, J., et al. (2024). Borehole and core measurement data for the rock mass characterization of ICDP expedition 5071, DIVE (Drilling the Ivrea-Verbano zonE), borehole 5071_1_B. *GFZ Data Services*. https://doi.org/10.5880/ICDP.5071.003

Liu, B., Kern, H., & Popp, T. (1997). Attenuation and velocities of P- and S-waves in dry and saturated crystalline and sedimentary rocks at ultrasonic frequencies. *Physics and Chemistry of the Earth*, *22*(1), 75–79. https://doi.org/10.1016/S0079-1946(97)00081-5

Lofts, J. C., & Bourke, L. T. (1999). The recognition of artefacts from acoustic and resistivity borehole imaging devices. *Geological Society, London, Special Publications*, *159*(1), 59–76. https://doi.org/10.1144/GSL.SP.1999.159.01.03

Lorenz, H., Rosberg, J.-E., Juhlin, C., Bjelm, L., Almqvist, B. S. G., Berthet, T., et al. (2015). COSC-1 – Drilling of a subduction-related allochthon in the Palaeozoic Caledonide orogen of Scandinavia. *Scientific Drilling*, *19*, 1–11. https://doi.org/10.5194/sd-19-1-2015

Lu, Y., Stehly, L., & Paul, A., & AlpArray Working Group. (2018). High-resolution surface wave tomography of the European crust and uppermost mantle from ambient seismic noise. *Geophysical Journal International*, *214*(2), 1136–1150. https://doi.org/10.1093/gji/ggy188

Lüschen, E., Bram, K., Söllner, W., & Sobolev, S. (1996). Nature of seismic reflections and velocities from VSP-experiments and borehole measurements at the KTB deep drilling site in southeast Germany. *Tectonophysics*, *264*(1–4), 309–326. https://doi.org/10.1016/S0040-1951(96)00134-5

Mahmoodi, O., & Smith, R. (2015). Clustering of downhole physical property measurements at the Victoria property, Sudbury for the purpose of extracting lithological information. *Journal of Applied Geophysics*, *118*, 145–154. https://doi.org/10.1016/j.jappgeo.2015.04.015

Maiti, S., & Tiwari, R. K. (2010). Neural network modeling and an uncertainty analysis in Bayesian framework: A case study from the KTB borehole site. *Journal of Geophysical Research*, *115*(B10). https://doi.org/10.1029/2010JB000864

Malusà, M. G., Guillot, S., Zhao, L., Paul, A., Solarino, S., Dumont, T., et al. (2021). The deep structure of the alps based on the CIFALPS seismic experiment: A synthesis. *Geochemistry, Geophysics, Geosystems*, *22*(3), e2020GC009466. https://doi.org/10.1029/2020GC009466

Mari, J.-L. (1994). *Full waveform acoustic data processing*. Editions TECHNIP.

Mavko, G., Mukerji, T., & Dvorkin, J. (2009). *The rock physics handbook: Tools for seismic analysis of porous media* (2nd ed.). Cambridge University Press. https://doi.org/10.1017/CBO9780511626753

Mehnert, K. R. (1975). The Ivrea Zone, a model of the deep crust. *Neues Jahrbuch für Mineralogie Abhandlungen*, *125*, 156–199.

Miller, K. G., Browning, J. V., Mountain, G. S., Bassetti, M. A., Monteverde, D., Katz, M. E., et al. (2013). Sequence boundaries are impedance contrasts: Core-seismic-log integration of Oligocene–Miocene sequences, New Jersey shallow shelf. *Geosphere*, *9*(5), 1257–1285. https://doi.org/10.1130/GES00858.1

Mooney, W. D., & Meissner, R. (1992). Multi-genetic origin of crustal reflectivity: A review of seismic reflection profiling of the continental lower crust and moho. In D. M. Fountain, R. Arculus, & R. W. Kay (Eds.), *Continental lower crust* (Vol. 23, pp. 45–79). Elsevier.

Musacchio, G., Zappone, A., Cassinis, R., & Scarascia, S. (1998). Petrographic interpretation of a complex seismic crust–mantle transition in the central-eastern Alps. *Tectonophysics*, *294*(1–2), 75–88. https://doi.org/10.1016/S0040-1951(98)00094-8

Niggli, E. (1947). Über den Zusammenhang zwischen der positiven Schwereanomalie am Südfuss der Westalpen und der Gesteinszone von Ivrea. https://doi.org/10.5169/SEALS-160786

Nur, A., & Simmons, G. (1969). The effect of saturation on velocity in low porosity rocks. *Earth and Planetary Science Letters*, *7*(2), 183–193. https://doi.org/10.1016/0012-821X(69)90035-1

Paillet, F. L., Barton, C., Luthi, S., Rambow, F., & Zemanek, J. R. (1990). *Borehole imaging and its application in well logging-an overview* (Vol. 6001, pp. 3–23). Borehole Imaging, Society of Professional Well Log Analysts, Inc.

Paillet, F. L., Keys, W. S., & Hess, A. E. (1985). Effects of lithology on televiewer-log quality and fracture interpretation. SPWLA 26th Annual Logging Symposium.

Pechnig, R., Haverkamp, S., Wohlenberg, J., Zimmermann, G., & Burkhardt, H. (1997). Integrated log interpretation in the German continental deep drilling program: Lithology, porosity, and fracture zones. *Journal of Geophysical Research*, *102*(B8), 18363–18390. https://doi.org/10.1029/96JB03802

Peressini, G., Quick, J. E., Sinigoi, S., Hofmann, A. W., & Fanning, M. (2007). Duration of a large mafic intrusion and heat transfer in the lower crust: A SHRIMP U-Pb zircon study in the Ivrea-Verbano zone (western alps, Italy). *Journal of Petrology*, *48*(6), 1185–1218. https://doi.org/10.1093/petrology/egm014

Pistone, M., Müntener, O., Ziberna, L., Hetényi, G., & Zanetti, A. (2017). Report on the ICDP workshop DIVE (drilling the Ivrea–Verbano zonE). *Scientific Drilling*, *23*, 47–56. https://doi.org/10.5194/sd-23-47-2017

Pistone, M., Ziberna, L., Hetényi, G., Scarponi, M., Zanetti, A., & Müntener, O. (2020). Joint geophysical-petrological modeling on the Ivrea geophysical body beneath Valsesia, Italy: Constraints on the continental lower crust. *Geochemistry, Geophysics, Geosystems*, *21*(12), e2020GC009397. https://doi.org/10.1029/2020GC009397

Popp, T., & Kern, H. (1994). The influence of dry and water saturated cracks on seismic velocities of crustal rocks-a comparison of experimental data with theoretical model. *Surveys in Geophysics*, *15*(5), 443–465. https://doi.org/10.1007/BF00690169

Quick, J. E., Sinigoi, S., & Mayer, A. (1995). Emplacement of mantle peridotite in the lower continental crust, Ivrea-Verbano zone, northwest Italy. *Geology*, *23*(8), 739–742. https://doi.org/10.1130/0091-7613(1995)023<0739:EOMPIT>2.3.CO;2

Quick, J. E., Sinigoi, S., Snoke, A. W., Kalakay, T. J., Mayer, A., & Peressini, G. (2003). *Geologic map of the southern Ivrea-Verbano zone, northwestern Italy*. USGS.

Redler, C., Johnson, T. E., White, R. W., & Kunz, B. E. (2012). Phase equilibrium constraints on a deep crustal metamorphic field gradient: Metapelitic rocks from the Ivrea Zone (NW Italy). *Journal of Metamorphic Geology*, *30*(3), 235–254. https://doi.org/10.1111/j.1525-1314.2011.00965.x

Rivalenti, G., Garuti, G., Rossi, A., Siena, F., & Sinigoi, S. (1981). Existence of different peridotite types and of a layered igneous complex in the Ivrea Zone of the Western Alps. *Journal of Petrology*, *22*(1), 127–153. https://doi.org/10.1093/petrology/22.1.127

Rutter, E., Brodie, K., James, T., & Burlini, L. (2007). Large-scale folding in the upper part of the Ivrea-Verbano zone, NW Italy. *Journal of Structural Geology*, *29*(1), 1–17. https://doi.org/10.1016/j.jsg.2006.08.013

Scarponi, M., Hetényi, G., Berthet, T., Baron, L., Manzotti, P., Petri, B., et al. (2020). New gravity data and 3-D density model constraints on the Ivrea geophysical body (western alps). *Geophysical Journal International*, *222*(3), 1977–1991. https://doi.org/10.1093/gji/ggaa263

Scarponi, M., Hetényi, G., Plomerová, J., Solarino, S., Baron, L., & Petri, B. (2021). Joint seismic and gravity data inversion to image intra-crustal structures: The Ivrea geophysical body along the Val Sesia profile (Piedmont, Italy). *Frontiers in Earth Science*, *9*. https://doi.org/10.3389/feart.2021.671412

Scarponi, M., Kvapil, J., Plomerová, J., Solarino, S., & Hetényi, G. (2024). New constraints on the shear wave velocity structure of the Ivrea geophysical body from seismic ambient noise tomography (Ivrea-Verbano Zone, Alps). *Geophysical Journal International*, *236*(2), 1089–1105. https://doi.org/10.1093/gji/ggad470

Schmid, R. (1967). Zur Petrographie und Struktur der Zone Ivrea-Verbano zwischen Valle d'Ossola und Val Grande (Prov. Novara, Italien), Schweizer. *Mineralogische und Petrographische Mitteilungen*, *47*, 935–1117.

Schmid, S. M., Zingg, A., & Handy, M. (1987). The kinematics of movements along the Insubric line and the emplacement of the Ivrea zone. *Tectonophysics*, *135*(1), 47–66. https://doi.org/10.1016/0040-1951(87)90151-X

Schnetger, B. (1994). Partial melting during the evolution of the amphibolite-to granulite-facies gneisses of the Ivrea Zone, northern Italy. *Chemical Geology*, *113*(1), 71–101. https://doi.org/10.1016/0009-2541(94)90006-X

Sinigoi, S., Antonini, P., Demarchi, G., Longinelli, A., Mazzucchelli, M., Negrini, L., & Rivalenti, G. (1991). Intractions of mantle and crustal magmas in the southern part of the Ivrea Zone (Italy). *Contributions to Mineralogy and Petrology*, *108*(4), 385–395. https://doi.org/10.1007/BF00303445

Sinigoi, S., Quick, J. E., Clemens-Knott, D., Mayer, A., Demarchi, G., Mazzucchelli, M., et al. (1994). Chemical evolution of a large mafic intrusion in the lower crust, Ivrea-Verbano Zone, northern Italy. *Journal of Geophysical Research*, *99*(B11), 21575–21590. https://doi.org/10.1029/94JB00114

Smithson, S. B., Wenzel, F., Ganchin, Y. V., & Morozov, I. B. (2000). Seismic results at Kola and KTB deep scientific boreholes: Velocities, reflections, fluids, and crustal composition. *Tectonophysics*, *329*(1), 301–317. https://doi.org/10.1016/S0040-1951(00)00200-6

Sun, S., Ji, S., Wang, Q., Xu, Z., Salisbury, M., & Long, C. (2012). Seismic velocities and anisotropy of core samples from the Chinese Continental Scientific Drilling borehole in the Sulu UHP terrane, eastern China. *Journal of Geophysical Research*, *117*(B1). https://doi.org/10.1029/2011JB008672

Suski, B., Ladner, F., Baron, L., Vuataz, F. D., Philippossian, F., & Holliger, K. (2008). Detection and characterization of hydraulically active fractures in a carbonate aquifer: Results from self-potential, temperature and fluid electrical conductivity logging in the Combioula hydro-thermal system in the southwestern Swiss alps. *Hydrogeology Journal*, *16*(7), 1319–1328. https://doi.org/10.1007/s10040-008-0302-5

The ECORS-CROP Deep Seismic Sounding Group. (1989). Mapping the Moho of the Western Alps by wide-angle reflection seismics. *Tectonophysics*, *162*(3–4), 193–202. https://doi.org/10.1016/0040-1951(89)90243-6

The ECORS-CROP Gravity Group. (1989). Gravity modelling along the ECORS-CROP vertical seismic reflection profile through the Western Alps. *Tectonophysics*, *162*(3–4), 203–218. https://doi.org/10.1016/0040-1951(89)90244-8

Tiab, D., & Donaldson, E. C. (2015). *Petrophysics: Theory and practice of measuring reservoir rock and fluid transport properties*. Gulf Professional Publishing.

Townend, J., Sutherland, R., Toy, V. G., Eccles, J. D., Boulton, C., Cox, S. C., & McNamara, D. (2013). Late-interseismic state of a continental plate-bounding fault: Petrophysical results from DFDP-1 wireline logging and core analysis, Alpine Fault, New Zealand. *Geochemistry, Geophysics, Geosystems*, *14*(9), 3801–3820. https://doi.org/10.1002/ggge.20236

Tsang, C. F., Hufschmied, P., & Hale, F. V. (1990). Determination of fracture inflow parameters with a borehole fluid conductivity logging method. *Water Resources Research*, *26*(4), 561–578. https://doi.org/10.1029/WR026i004p00561

Vernik, L., Hickman, S., Lockner, D., & Rusanov, M. (1994). Ultrasonic velocities in cores from the Kola superdeep well and the nature of subhorizontal seismic reflections. *Journal of Geophysical Research*, *99*(B12), 24209–24219. https://doi.org/10.1029/94JB01236

Voshage, H., Hofmann, A. W., Mazzucchelli, M., Rivalenti, G., Sinigoi, S., Raczek, I., & Demarchi, G. (1990). Isotopic evidence from the Ivrea Zone for a hybrid lower crust formed by magmatic underplating. *Nature*, *347*(6295), 731–736. https://doi.org/10.1038/347731a0

Wang, W., Schmitt, D. R., & Chan, J. (2023). Heterogeneity versus anisotropy and the state of stress in stable cratons: Observations from a deep borehole in Northeastern Alberta, Canada. *Journal of Geophysical Research: Solid Earth*, *128*(3), e2022JB025287. https://doi.org/10.1029/2022JB025287

Wang, X.-Q., Schubnel, A., Fortin, J., David, E. C., Guéguen, Y., & Ge, H.-K. (2012). High Vp/Vs ratio: Saturated cracks or anisotropy effects? *Geophysical Research Letters*, *39*(11). https://doi.org/10.1029/2012GL051742

Wasilewski, P., & Fountain, D. M. (1982). The Ivrea Zone as a model for the distribution of magnetization in the continental crust. *Geophysical Research Letters*, *9*(4), 333–336. https://doi.org/10.1029/GL009i004p00333

Waters, C., Tikoff, B., Goodwin, L. B., & Little, T. A. (2003). Ductile instabilities and structural heterogeneity in the lower continental crust. In J. A. Goff & K. Holliger (Eds.), *Heterogeneity in the crust and upper mantle: Nature, scaling, and seismic properties* (pp. 1–36). Springer US. https://doi.org/10.1007/978-1-4615-0103-9_1

Wepfer, W. W., & Christensen, N. I. (1991). A seismic velocity-confining pressure relation, with applications. *International Journal of Rock Mechanics and Mining Sciences & Geomechanics Abstracts*, *28*(5), 451–456. https://doi.org/10.1016/0148-9062(91)90083-X

Williams, J. H., & Johnson, C. D. (2004). Acoustic and optical borehole-wall imaging for fractured-rock aquifer studies. *Journal of Applied Geophysics*, *55*(1), 151–159. https://doi.org/10.1016/j.jappgeo.2003.06.009

Williams, M. A., Kelsey, D. E., & Rubatto, D. (2022). Thorium zoning in monazite: A case study from the Ivrea–Verbano zone, NW Italy. *Journal of Metamorphic Geology*, *40*(6), 1015–1042. https://doi.org/10.1111/jmg.12656

Williams, M. C., Shive, P. N., Fountain, D. M., & Ronald Frost, B. (1985). Magnetic properties of exposed deep crustal rocks from the Superior Province of Manitoba. *Earth and Planetary Science Letters*, *76*(1), 176–184. https://doi.org/10.1016/0012-821X(85)90157-8

Wolter, K. E., & Berckhemer, H. (1989). Time dependent strain recovery of cores from the KTB — Deep drill hole. *Rock Mechanics and Rock Engineering*, *22*(4), 273–287. https://doi.org/10.1007/BF01262283

Xu, Z., Yang, J., Wang, C., An, Z., Li, H., Wang, Q., & Su, D. (2017). Fifteen years of the Chinese continental scientific drilling program. *Scientific Drilling*, *22*, 1–18. https://doi.org/10.5194/sd-22-1-2017

Yang, M.-S., Wu, K.-L., Hsieh, J.-N., & Yu, J. (2008). Alpha-cut implemented fuzzy clustering algorithms and switching regressions. *IEEE Transactions on Systems, Man, and Cybernetics, Part B (Cybernetics)*, *38*(3), 588–603. https://doi.org/10.1109/TSMCB.2008.915537

Zang, A., Wolter, K., & Berckhemer, H. (1989). Strain recovery, microcracks and elastic anisotropy of drill cores from KTB deep well. *Strain Recovery, Microcracks and Elastic Anisotropy of Drill Cores from KTB Deep Well*, *1*(3), 115–126.

Zemanek, J., Caldwell, R. L., Glenn, E. E., Holcomb, S. V., Norton, L. J., & Straus, A. J. D. (1969). The borehole TelevieweA new logging concept for fracture location and other types of borehole inspection. *Journal of Petroleum Technology*, *21*(06), 762–774. https://doi.org/10.2118/2402-PA

Zhou, Z., Caspari, E., Barbosa, N. D., Greenwood, A., & Holliger, K. (2022). Mechanical compliance of individual fractures in a heterogeneous rock mass from production-type full-waveform sonic data. *Journal of Geophysical Research: Solid Earth*, *127*(8), e2022JB024302. https://doi.org/10.1029/2022JB024302

Zingg, A. (1983). The Ivrea and Strona-Ceneri zones (southern alps, Ticino and N-Italy)—A review. *Schweizerische Mineralogische Und Petrographische Mitteilungen = Bulletin Suisse de Minéralogie et Pétrographie = Bollettino Svizzero Di Mineralogia e Petrografia*, *63*(2–3), 361. https://doi.org/10.5169/seals-48742

Zoback, M. D., Moos, D., Mastin, L., & Anderson, R. N. (1985). Well bore breakouts and in situ stress. *Journal of Geophysical Research*, *90*(B7), 5523–5530. https://doi.org/10.1029/JB090iB07p05523